J. Fluid Mech. (1990), *vol.* 216, *pp.* 35–70
Printed in Great Britain

Thermal dispersion from a line source in the shearless turbulence mixing layer

By S. VEERAVALLI† AND Z. WARHAFT
Sibley School of Mechanical and Aerospace Engineering, Cornell University, Ithaca, NY 14853, USA

(Received 18 July 1989 and in revised form 9 November 1989)

We experimentally investigate dispersion from a heated line source placed in the central region of a turbulence mixing layer. Recently described by Veeravalli & Warhaft (1989) the mixing layer has no mean shear and consists of gradients in the velocity variance and scale; it is formed from a composite grid of constant solidity from which two distinct velocity scales are formed, one on either side of the stream. Mixing is effected by intermittent turbulent penetration and diffusion. The dispersion measurements were carried out in the convective regime where both plume flapping and fine-scale turbulent mixing play a role, the latter becoming more dominant as the plume evolves. The mean and variance temperature profiles are strongly skewed (with larger tails on the low turbulence side of the flow) in the earlier stages of the plume development. Here, in the convective range, the median and peak of the mean plume are deflected toward the large-scale region. As the flow evolves the profiles become more symmetrical but as the plume enters the turbulent diffusive stage there is evidence that the profiles again became asymmetric but now with longer tails in the high turbulence side of the flow (owing to the higher diffusivity). The temperature variance and heat flux budgets are highly asymmetric but tend to exhibit many of the characteristics of the budget of a line source in decaying homogeneous grid turbulence which is also presented here. However, a distinct region of negative production (counter-gradient heat flux) is found in the temperature variance budget and this is shown to be a consequence of the asymmetry of the transverse velocity probability density function in the mixing layer. Temperature spectra, both of the time series and of the intermittency function, across the plume are described. They are shown to peak at high wavenumbers in the centre and edge of the plume and at lower wavenumbers in the intermediate region. Their form is shown to change as the plume develops fine-scale structure and flapping becomes less important.

1. Introduction

Predicting mixing and dispersion rates of scalar contaminants in turbulent flows remains an outstanding problem and one of great practical interest because of increased environmental emissions (both planned and accidental) and because of concern over the design of efficient mixing and combustion devices. In practice, dispersion usually occurs in time dependent inhomogeneous flows (such as the atmospheric boundary layer or the internal combustion engine); flows that are

† Present address: Center for Turbulence Research, Stanford University, Stanford, CA 94305, USA.

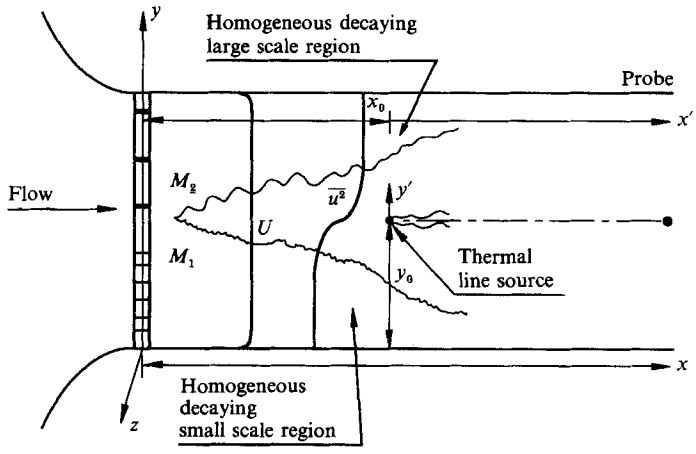

FIGURE 1. Sketch of the wind tunnel showing the parallel bar grid consisting of two different mesh lengths. $M_1 < M_2$ (a biplanar constant mesh bar grid was also used, see text). Also shown are typical mean (U) and variance ($\overline{u^2}$) profiles, the position of the line source and the coordinate system. After Veeravalli & Warhaft (1989).

beyond the reach of analytical models or direct numerical solution of the exact equations. They are also extremely difficult to measure, be they in the field or laboratory, partly because of the large number of parameters that must be varied to make the study comprehensive. Furthermore, detailed measurements of these complex flows do not emphasize key concepts or single out particular mechanisms because there are so many interacting processes at work. Indeed, it is an important challenge for the experimenter to investigate flows that are simple (but not trivial) so as to clearly elucidate basic mechanisms yet at the same time provide insight and impetus to the study of practically interesting phenomena such as geophysical and industrial mixing and dispersion.

There is another factor that strongly determines the nature and conduct of the modern fluid mechanics experiment. Using large computers, direct numerical simulation of turbulent flows is becoming an attractive alternative and may well prove cheaper and provide more details than experiments in the future. Yet the computationalist must rely heavily on the experimenter in setting up the conditions that match those of reality. Possibly, in time, the experiment will assume a more exploratory (rather than archival) role, determining the type of flow that the computationalist will explore in detail. Yet here too, there are limits, placed on the size of the largest computer. Even the most sanguine of computationalists expresses doubt about a complete dispersion calculation of say a cubic kilometre of the atmospheric boundary layer (with approximately 10^{18} grid points) in the foreseeable future. In spite of rapid advances in both computation and theory, turbulence still remains an experimentally based discipline.

It is such considerations that provided the impetus for the experiment to be described here. The flow is the turbulence mixing layer. It is formed in decaying grid turbulence in which the mean fluid velocity is constant throughout but two distinct scales of turbulence are formed on either side of the stream. In order to study scalar dispersion, a thermal line source was inserted at the centre of the mixing layer (figure 1). We have recently completed a detailed study of the velocity field for this

flow (Veeravalli & Warhaft 1989, hereinafter referred to as VW†) and in this paper we focus on scalar dispersion. As discussed in VW, this flow is of theoretical importance because it highlights the interaction of two turbulence-containing scales with their energy at different wavenumbers. Simple turbulence models are unable to predict such a flow and there is a need for experimental insight to aid more complex modelling and computer simulations.

Apart from its fundamental importance the mixing layer is also paradigmatic of a number of practical flows. Consider, for example, a turbulent reaction chamber in which two reactants, each having a different turbulence scale are co-flowing at the same mean speed into the reaction chamber. Here the mixing of the reactants is solely determined by the turbulence – turbulence interactions. Or consider a turbulent boundary layer evolving in co-flowing turbulence. The outer-edge of the boundary layer is almost shearless and thus the interaction of the two scales (one determined by the depth of the boundary layer and the other by the free-stream turbulence) is again similar in many respects to our experiment.

The addition of a thermal line source to the flow both aids in an understanding of the flow itself (since the thermal field is passive it acts like a dye) and provides needed information on scalar mixing. Both the flows of practical interest mentioned above invariably involve scalar mixing (indeed the reaction chamber's sole purpose is to mix scalars). We note that even if the velocity field of a turbulent flow can be completely described we still have great difficulty in determining the scalar mixing characteristics even though the diffusion equation is linear (for the scalar). The problem is partly due to the disparate scales of the scalar and velocity fields.

Stemming from the earlier work of Uberoi & Corrsin (1953) and Townsend (1954) there have been a number of recent experiments concerning line- and point-source dispersion in turbulent flows. Thus Warhaft (1984) and Stapountzis *et al.* (1986) have re-examined line-source dispersion, and Nakamura, Sakai & Miyata (1987) have studied point-source dispersion, in decaying grid turbulence. Karnik & Tavoularis (1989) have investigated line-source dispersion in a uniformly sheared turbulent flow and Fackrell & Robins (1982) have investigated a point source in the turbulent boundary layer. Lamb (1982) and Hunt (1982, 1985) provide an overview of diffusion from sources in these more complex flows. The study to be presented here combines some of the characteristics of diffusion in a complex flow like the boundary layer, where the velocity variance and scale varies with height, but does not have the added complexity of mean shear and in this sense provides a bridge between the experiment of Fackrell & Robins and the more simple grid-turbulence experiments mentioned above.

The outline of the paper is as follows. In the next section we describe the governing equations for the thermal field (the equations for the velocity field are given in VW). In §3 the experimental apparatus is described. Section 4 provides a summary of the velocity field and is concerned mainly with those aspects relevant to the scalar dispersion problem (for full details of the velocity field see VW). The remainder of the paper (§5) is on the line-source dispersion. First, new measurements of a line source in homogeneous (single scale) grid turbulence are described. These supplement those

† Gilbert (1980) has also experimentally studied this flow although only in the limiting case in which the velocity field is Gaussian and spreading is caused by turbulent diffusion. In VW the lengthscale ratio is sufficiently great such that large-scale intermittency as well as turbulent diffusion affect the mixing. Thus the velocity field is non-Gaussian having large skewness and kurtosis.

of Warhaft (1984) and will be used to contrast with those of the mixing layer. In particular, new measurements of variance budgets and spectra are presented. Then the line source measurements in the mixing layer are described. Initial conditions are varied by using two, parallel bar grids (of mesh ratios 3.3:1 and 8.9:1), and a perforated plate (VW). The positioning of the line source from the grid is also varied. Mean, and r.m.s. profiles, variance budgets and spectra are documented and related to physical models.

2. The governing equations

Figure 1 shows a schematic diagram of the experimental set-up and the coordinate system used. In the equations below, Θ denotes the excess mean temperature (above the ambient), while θ denotes temperature fluctuations. The mean velocity field is represented by $\boldsymbol{U} = (U, 0, 0)$ and the fluctuating velocity by $\boldsymbol{u} = (u, v, w)$. The notation $\boldsymbol{x} = (x, y, z)$ and $\boldsymbol{u} = (u, v, w)$ will be used interchangeably with $\boldsymbol{x} = (x_1, x_2, x_3)$ and $\boldsymbol{u} = (u_1, u_2, u_3)$. Assuming constant heat capacity, thermal diffusivity, α, and viscosity, ν, the governing equation for the mean temperature field is given by:

$$U\frac{\partial \Theta}{\partial x}+\frac{\partial \overline{u\theta}}{\partial x}+\frac{\partial \overline{v\theta}}{\partial y}=\alpha\left[\frac{\partial^2\Theta}{\partial y^2}+\frac{\partial^2\Theta}{\partial x^2}\right]. \tag{1}$$

Hence,

$$\frac{\mathrm{d}}{\mathrm{d}x}\int_{-\infty}^{\infty}(U\Theta+\overline{u\theta})\,\mathrm{d}y=0, \tag{2}$$

and therefore,

$$\int_{-\infty}^{\infty}\left(\Theta+\frac{\overline{u\theta}}{U}\right)\mathrm{d}y\approx\int_{-\infty}^{\infty}\Theta\,\mathrm{d}y=\text{constant}. \tag{3}$$

Homogeneity in the z-direction has been assumed in the above equations.

The evolution of the centre of mass of the mean temperature field

$$Y_c\left(\equiv\int_{-\infty}^{\infty}\Theta y\,\mathrm{d}y\Big/\int_{-\infty}^{\infty}\Theta\,\mathrm{d}y\right),$$

which is also the location of the median temperature, may be obtained thus: from (1) it follows that,

$$U\frac{\mathrm{d}}{\mathrm{d}x}\int_{-\infty}^{\infty}\Theta y\,\mathrm{d}y=\int_{-\infty}^{\infty}\overline{v\theta}\,\mathrm{d}y, \tag{4}$$

(assuming $\overline{u\theta}\ll U\Theta$) and hence,

$$\frac{\mathrm{d}}{\mathrm{d}x}Y_c=\left(\int_{-\infty}^{\infty}\overline{v\theta}\,\mathrm{d}y\Big/U\int_{-\infty}^{\infty}\Theta\,\mathrm{d}y\right). \tag{5}$$

In homogeneous turbulence, the right-hand side of (5) is zero by symmetry and hence, the expected result, $Y_c = \text{constant} = y_0$, is recovered. However, when the turbulence is inhomogeneous, $\int_{-\infty}^{\infty}\overline{v\theta}\,\mathrm{d}y$ need not be zero and hence the mean temperature profile could shift laterally. This is discussed further in §5 below.

The equation for the temperature variance, $\overline{\theta^2}$, is:

$$0=-U\frac{\partial}{\partial x}\frac{\overline{\theta^2}}{2}-\frac{\partial}{\partial y}\frac{\overline{\theta^2 v}}{2}-\overline{\theta v}\frac{\partial\Theta}{\partial y}-\alpha\overline{\frac{\partial\theta}{\partial x_j}\frac{\partial\theta}{\partial x_j}}. \tag{6}$$

advection transport production destruction

Each of the terms in (6) tends to zero as $y \to \pm\infty$, in both homogeneous and inhomogeneous turbulence, while each term is symmetric about the source location, y_0, only in homogeneous turbulence.

The budget for the principal component of the heat flux vector, $\overline{\theta v}$, is:

$$0 = -U\frac{\partial}{\partial x}\overline{\theta v} - \frac{\partial}{\partial y}\overline{\theta v^2} - \overline{v^2}\frac{\partial \Theta}{\partial y} - \frac{1}{\rho}\overline{\theta\frac{\partial p}{\partial y}}. \tag{7}$$

advection transport production pressure

The molecular smearing term $(\nu+\alpha)(\overline{\partial\theta\,\partial v/\partial x_j\,\partial x_j})$ has been dropped since it is negligible at high Reynolds numbers (local isotropy of small scales) and hence the pressure term is chiefly responsible for the destruction of $\overline{\theta v}$. In homogeneous turbulence $\overline{\theta v}$ is antisymmetric about y_0 and so are all the other terms in (7).

3. Apparatus and flow realization

The experiments were conducted in the same low-speed, vertically oriented wind tunnel as used by VW (see also Sirivat & Warhaft 1983). It has a test section 4.25 m in length and a cross-section of $0.406 \times 0.406\ \mathrm{m}^2$. For most of the experiments described here, the inhomogeneous velocity field was generated by means of a parallel bar grid with a mesh ratio (M_2/M_1) of 3.3:1. (The subscript '1' characterizes the homogeneous low intensity edge of the inhomogeneous turbulence field, while the subscript '2' characterizes the homogeneous high intensity edge.) The grid bars were square-sectioned of side 3.18 mm and 9.53 mm and the mesh sizes were 9.53 mm and 31.5 mm respectively, yielding a grid solidity (ratio of the closed area to the total area) σ, of 0.32. Two other inhomogeneous grids were also used; (*a*) a parallel bar grid of mesh ratio 8.9:1 and (*b*) a perforated plate with a mesh ratio of 3:1. All three grids are described in detail in VW. The measurements described here were carried under exactly the same conditions as in VW; the velocity fields are documented in that paper. In addition, measurements were also made in a homogeneous velocity field, generated by a bi-planar grid of mesh size $M = 25.0$ mm and solidity 0.34. These measurements complement those of Warhaft (1984) and both will be compared with our measurements for the inhomogeneous velocity field. The mean velocity in all the cases was approximately 6 m/s (table 1). Table 1 documents mesh sizes, solidity and flow parameters for all the grids mentioned above.

To generate the thermal line sources, Constantan wires of diameter 0.076 mm and Chromel wires of diameter 0.127 mm were used. The source was located either at $x_0 = 31.5$ cm or 62.4 cm downstream of the grid. The locations correspond to $10M_2$ and $19.8M_2$ respectively, based on the mesh size of the 3.3:1 bar grid. The lateral position y_0 (figure 1) was approximately the inflection point of the kinetic energy profile for each of the inhomogeneous velocity fields. For reasons explained below, two different source strengths, 19 and 29.5 W/m, were used for the 0.076 mm diameter wire, while, the 0.127 mm diameter wire was operated at approximately 127 W/m. The wires were threaded through small holes in the tunnel walls and wound around spools placed outside the tunnel, which were tightened, after heating the wires, in order to prevent sagging. The cold-wire Reynolds numbers were 28 and 46, with corresponding hot-wire Reynolds numbers of approximately 21 and 28, thus precluding the possibility of vortex shedding (Zdravkovich 1969). The various wire diameters and source strengths were necessitated by the conflicting requirements of a large

Flow parameters	Bi-planar grid	3.3:1 Parallel bar grid	8.9:1 Parallel bar grid	3:1 Perforated plate
M_1 (cm)	2.5	0.95	0.477	1.12
M_2 (cm)	—	3.15	4.25	3.35
Solidity σ	0.34	0.32	0.29	0.31
Location of the geometric centre (cm)	—	18.24	14.4	20.04
Mean velocity U (m/s)	5.9	5.9	5.85	5.8
$R_{M_1} \equiv UM_1/\nu$	9219	3505	1744	4060
$R_{M_2} \equiv UM_2/\nu$	—	11616	15539	12180
$k_1 \equiv \frac{1}{2}(\overline{u_1^2}+\overline{v_1^2}+\overline{w_1^2})$ (m^2/s^2)	0.061	0.028	0.0091	0.0082
$\epsilon_1 = -\mathrm{d}k_1/\mathrm{d}t$ (m^2/s^3)	0.781	0.365	0.103	0.090
$l_1 \equiv k_1^{\frac{3}{2}}/\epsilon_1$ (cm)	1.93	1.27	0.84	0.80
$k_2 \equiv \frac{1}{2}(\overline{u_2^2}+\overline{v_2^2}+\overline{w_2^2})$ (m^2/s^2)	—	0.172	0.222	0.051
$\epsilon_2 = -\mathrm{d}k_2/\mathrm{d}t$ (m^2/s^3)	—	2.31	2.81	0.655
$l_2 \equiv k_2^{\frac{3}{2}}/\epsilon_2$ (cm)	—	3.09	3.72	1.78
$\lambda_1 \equiv (\overline{u_1^2})^{\frac{1}{2}}/(\epsilon_1/15\nu)^{\frac{1}{2}}$ (cm)	0.38	0.37	0.38	0.42
$\lambda_2 \equiv (\overline{u_2^2})^{\frac{1}{2}}/(\epsilon_2/15\nu)^{\frac{1}{2}}$ (cm)	—	0.36	0.39	0.37
$R_{l_1} \equiv l_1(\overline{u_1^2})^{\frac{1}{2}}/\nu$	260	115	41.5	40.3
$R_{l_2} \equiv l_2(\overline{u_2^2})^{\frac{1}{2}}/\nu$	—	677	976.5	214
$R_{\lambda_1} \equiv \lambda_1(\overline{u_1^2})^{\frac{1}{2}}/\nu$	51.3	33.5	18.8	21.2
$R_{\lambda_2} \equiv \lambda_2(\overline{u_2^2})^{\frac{1}{2}}/\nu$	—	78.9	102.4	44.5
$\tau_1 \equiv k_1/\epsilon_1$ (s)	0.078	0.076	0.088	0.091
$\tau_2 \equiv k_2/\epsilon_2$ (s)	—	0.074	0.079	0.078
τ_1/τ_2	—	1.03	1.11	1.17
l_2/l_1	—	2.43	4.43	2.23

TABLE 1. Flow parameters for the four grids: k, ϵ and l are the turbulent kinetic energy, dissipation rate and integral length scale respectively; R_l and R_λ are the integral scale and Taylor Reynolds numbers based on l and the Taylor microscale λ respectively; and τ is the integral timescale. Subscript 1 refers to the small-scale homogeneous region, while subscript 2 refers to the large scale homogeneous region for the composite grid. For the homogeneous bi-planar grid only subscript 1 is used. The fluctuation parameters were evaluated at; (*a*) $x = 24.96M_1$ (62.4 cm) for the bi-planar grid using the decay laws from Warhaft (1984); (*b*) $x = 19.8M_2$ (62.4 cm) for the 3.3:1 bar grid; (*c*) $x = 14.68M_2$ (62.4 cm) for the 8.9:1 bar grid; and (*d*) $x = 19.4M_2$ (65 cm) for the perforated plate. (As noted in VW, the decay laws for the 8.9:1 bar grid could not be measured and thus the values reported here for the 8.9:1 bar grid are less accurate than those for the other grids.)

temperature signal and negligible disturbance of the velocity field. The mean velocity in the wake of the wire requires about 250 diameters to recover to within 99% of the free-stream value (Kellogg & Corrsin 1980), hence the fine wire, maintained at a strength of 29.5 W/m, was used for measurements close to the source ($x' \leqslant 4M_2$). The evolution at larger x' was obtained using the thicker wire at a strength of 127 W/m. As shown below, data obtained with the different wire diameters and source strengths agree well with each other.

Temperature fluctuations were measured with a 1.27 μm platinum wire with a length-to-diameter ratio $L/D \approx 400$, used in conjunction with an a.c. temperature bridge with a frequency response of 2.5 kHz. The probe current was approximately 0.6 mA. The prong spacing was greater than $3L$ thus alleviating the problem of probe–prong interaction. The temperature wire was calibrated using a 76.2 μm diameter Chromel–Constantan thermocouple. The probe arrangement was similar to the one described in Warhaft (1984), with the temperature wire positioned parallel

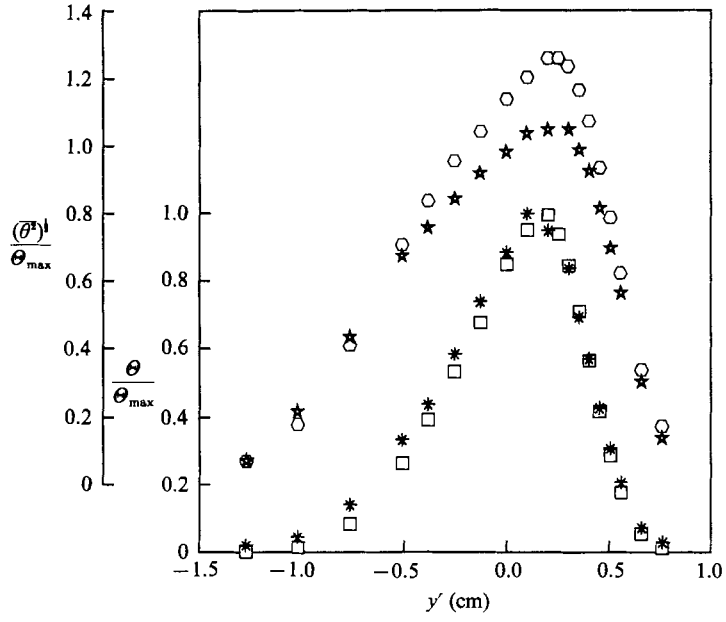

FIGURE 2. The normalized mean (Θ/Θ_{max}) and r.m.s. ($(\overline{\theta^2})^{\frac{1}{2}}/\Theta_{max}$) temperature profiles at $x' =$ 6.4 cm ($x_0 = 62.4$ cm) for the 3.3:1 bar grid. □ and *; mean profiles for the fine wire with low heating (0.0762 mm, 19 W/m) and thick wire with high heating (0.127 mm, 127 W/m) respectively. ○ and ☆; r.m.s. profiles for the fine and thick wire respectively.

to the line source in order to resolve accurately temperature moment profiles close to the source. The velocity field was measured using conventional X-hot wires in conjunction with Dantec 55M01 constant temperature bridges. The wires were made of tungsten with a diameter of 3.05 μm and a length to diameter ratio, L/D, of approximately 200. The hot wires were operated at an overheat ratio of 1.8. The velocity signals were band-pass filtered with Khronhite 3342 filters prior to digitization, however, the temperature signal was only low-pass filtered in order to accurately resolve the regions of sharp transition from the ambient to plume temperature. The calibration procedure for inclined wires, outlined by Champagne & Sleicher (1967) and Champagne, Sleicher & Wehrmann (1967) was modified to compensate for temperature contamination of the hot-wire data. This correction is essential especially when estimating correlations of u and θ (Perry 1982). The calibration scheme worked very well far away from the source ($x' \geqslant 10M_2$). However, close to the source, when the instantaneous plume width is comparable to the spacing between X and temperature wires (approximately 1.4 mm in our case), it is not possible to compensate for temperature contamination because the X and temperature wires could be in different regions of the instantaneous thermal plume. Hence, for the heat flux measurements close to the heated wire ($x'/x_0 < 0.2$) a very low source strength (19 W/m) was chosen in order to minimize contamination of the velocity data. For this low heating, accurate measurements of v could be obtained even without temperature compensation and since the velocity field is essentially identical at the X and temperature wires, their spacing being comparable to the Kolmogorov scale, accurate estimates of $v-\theta$ correlations could be obtained. The data analysis procedure is outlined in VW. Here we add that 100 blocks of data

consisting of 1024 and 2048 points were used for variance and spectra calculations respectively.

Figure 2 shows normalized mean and r.m.s. temperature profiles at $x' = 6.4$ cm ($x_0 = 62.4$ cm) for the 3.3:1 bar grid, obtained for the fine wire maintained at a source strength of 19 W/m and the thick wire operated at a strength of 127 W/m. The two mean profiles show very good agreement. The profile is marginally wider for the higher intensity source due to both the larger initial size and higher thermal diffusivity. The widths of the r.m.s. profiles also agree well with each other, however, the peak values differ by about 15%. This behaviour is consistent with the measurements of Warhaft (1984) and Stapountzis *et al.* (1986). We note that further from the source the agreement between the two cases improves, as the influence of the initial conditions diminishes. This is evident from figures 13 and 15 below (see §5.2).

4. The velocity field

The thermal dispersion measurements to be described here were carried out in homogeneous grid turbulence and in the shearless turbulence mixing layer. The velocity field for both the flows have been previously measured, the former by Warhaft (1984) and the latter by VW. In this section we document the salient features of these velocity fields. For further details the reader is referred to the above mentioned papers.

4.1. *The homogeneous velocity field*

New measurements of the velocity field for this case were not made, however, at the locations where the temperature field was measured, the data were found to be in very good agreement with the measurements of Warhaft (1984), who used the same grid (2.5 cm bi-planar) but a slightly larger mean velocity. The values of $\overline{u^2}$ agreed to within 3% with those estimated from the decay law reported in Warhaft (1984), while, $\overline{v^2}$ agreed to within 6%. Thus in order to facilitate comparison with the extensive measurements of Warhaft (1984), we will use his decay laws which are:

$$\frac{\overline{u^2}}{U^2} = 0.121\left(\frac{x}{M}\right)^{-1.4}, \quad \frac{\overline{v^2}}{U^2} = 0.076\left(\frac{x}{M}\right)^{-1.32}. \tag{8}$$

We note that variance measurements in flows such as this do not reproduce themselves to better than 5% accuracy.

The parameters describing the velocity field are presented in table 1.

4.2. *The turbulence mixing layer*

The velocity field produced by the 3.3:1 parallel bar grid consists of two regions of homogeneous turbulence of different intensities, separated by a mixing layer. However, the spacing between the grid bars is adjusted so as to produce a uniform pressure drop across the grid and hence the mean velocity field is constant across the entire flow (VW). Profiles of $\overline{u^2}$, $\overline{v^2}$ and $\overline{w^2}$ for the 3.3:1 parallel bar grid are shown in figure 3. The measurements were made at $x = 21.2M_2$ (66.7 cm). The arrows on the figure refer to the inflection points of variance profiles (I_u, I_v and I_w), and the geometric centre (position where the grid changes from one mesh size to the other)

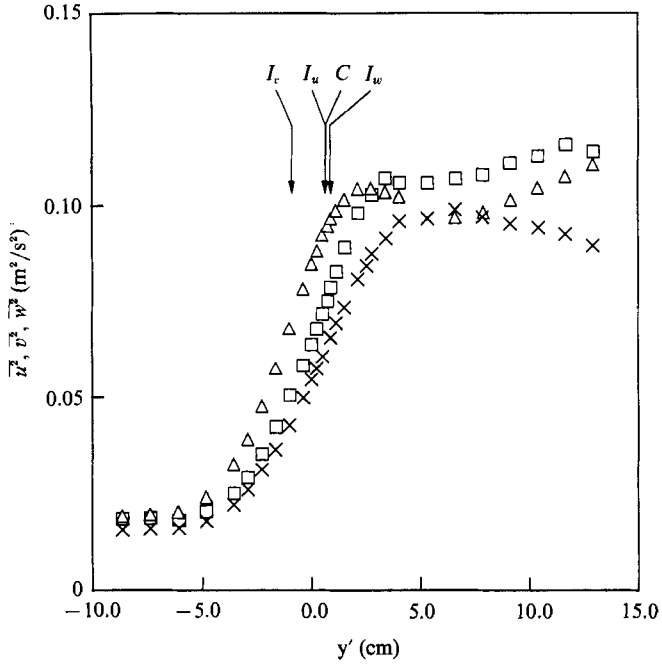

FIGURE 3. Profiles of $\overline{u^2}$, $\overline{v^2}$ and $\overline{w^2}$ for the 3.3:1 parallel bar grid at $x = 21.2M_2$ (66.7 cm from the grid). Arrows marked I_u, I_v and I_w refer to inflection points of the $\overline{u^2}$, $\overline{v^2}$, and $\overline{w^2}$, profiles and C is the geometrical centre of the grid (position where mesh size changes). □, $\overline{u^2}$; △, $\overline{v^2}$; ×, $\overline{w^2}$.

of the grid, C. The decay laws for the velocity variances in the two homogeneous regions (one on either side of the mixing layer) are (VW):

$$\frac{\overline{u_1^2}}{U^2} = 0.151\left(\frac{x}{M_1}\right)^{-1.33}, \quad \frac{\overline{u_2^2}}{U^2} = 0.167\left(\frac{x}{M_2}\right)^{-1.29}, \tag{9a}$$

$$\frac{\overline{v_1^2}}{U^2} = 0.130\left(\frac{x}{M_1}\right)^{-1.30}, \quad \frac{\overline{v_2^2}}{U^2} = 0.303\left(\frac{x}{M_2}\right)^{-1.51}, \tag{9b}$$

$$\frac{\overline{w_1^2}}{U^2} = 0.251\left(\frac{x}{M_1}\right)^{-1.49}, \quad \frac{\overline{w_2^2}}{U^2} = 0.282\left(\frac{x}{M_2}\right)^{-1.53}, \tag{9c}$$

$$\frac{k_1}{U^2} = 0.268\left(\frac{x}{M_1}\right)^{-1.39}, \quad \frac{k_2}{U^2} = 0.343\left(\frac{x}{M_2}\right)^{-1.42}, \tag{9d}$$

In the equations above k refers to the turbulent kinetic energy $\frac{1}{2}(\overline{u^2}+\overline{v^2}+\overline{w^2})$. The subscripts 1 and 2 refer to the high and low intensity sides of the mixing layer respectively. These results are the same as in VW since the thermal line source was placed in the same velocity field as that described in VW. In fact, some of the velocity field data presented in VW, were obtained from the joint velocity temperature measurements made with the line source present.

As shown in VW the v fluctuations form the primary mode of transport in the turbulence mixing layer. Figure 4(*a*) shows the variation of the skewness (normalized third moment $\overline{v^3}/(\overline{v^2})^{\frac{3}{2}}$) of v fluctuations, S_v, at $x = 21.2M_2$ (66.7 cm). We see that S_v

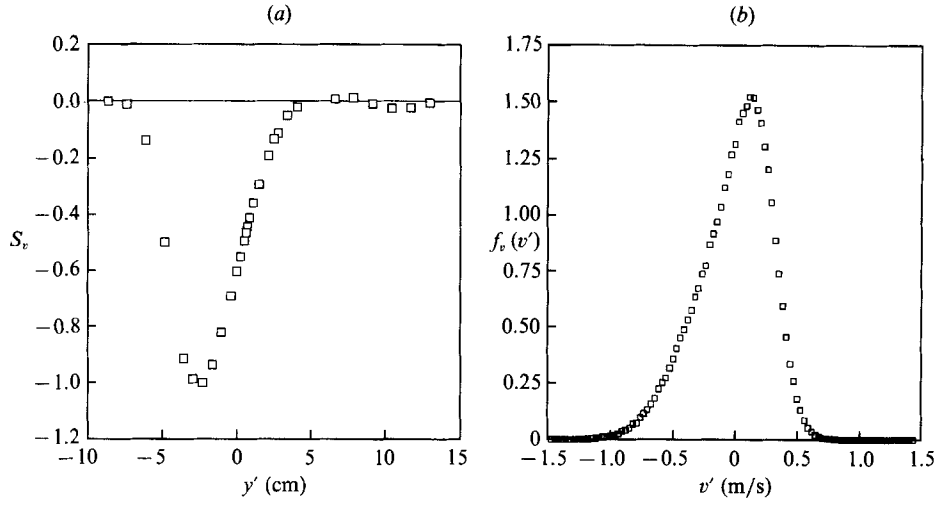

FIGURE 4. The skewness (*a*) and p.d.f. (*b*) of the transverse velocity, v, at $x = 21.2M_2$ (66.7 cm), $y = y_0$ for the 3.3:1 parallel bar grid.

is essentially zero in the homogeneous edges of the mixing layer. However, within the mixing layer S_v attains large negative values. This is because, within the mixing layer, fluctuations arising from the large-scale side are more likely to be negative and hence large deviations of the fluctuating v component from its mean, are more likely to be negative. Figure 4(*b*) shows the probability density function of v fluctuations, $f_v(v')$, obtained at $x = 21.2M_2$ (66.7 cm) and $y = y_0$ (note that this is approximately at the location of the line source placed at $x_0 = 19.8M_2$ and directly downstream of the one placed at $x_0 = 10M_2$). The asymmetry discussed above is clearly evident in the p.d.f. and it shows a significantly longer negative tail. This asymmetry of the velocity fluctuations has a profound effect on the mixing of the thermal plume in the turbulent convective region as is shown in §5.2 below. Turbulence parameters for this flow as well as those of the 8.9:1 parallel bar grid and the perforated plate, are documented in table 1.

5. The thermal line source dispersion

5.1. *Dispersion from the line source in homogeneous turbulence*

The evolution of a line source in homogeneous turbulence has been studied rather extensively, both experimentally and theoretically since the classical works of Taylor (1921, 1935); the most recent experiments having been carried out by Warhaft (1984) and Stapountzis *et al.* (1986). When the thermal source size is smaller than the Kolmogorov lengthscale, the evolution shows three distinct stages (Warhaft 1984; Anand & Pope 1983): molecular diffusive ($t \ll \alpha/\overline{v^2}$) wherein the plume width increases as $t^{\frac{1}{2}}$; turbulent-convective ($\alpha/\overline{v^2} \ll t \ll t_L$ where t_L is the Lagrangian timescale) where the width increases linearly with t, and turbulent-diffusive ($t \gg t_L$) where the plume width increases as $t^{1-\frac{1}{2}n}$, where n is the decay exponent of $\overline{v^2}$. We will present new measurements of the temperature variance budgets and spectra, obtained in the turbulent-convective range, which, to the best of our knowledge have not previously been documented in the literature. They will serve as a reference for similar measurements carried out in the inhomogeneous mixing layer to be described below.

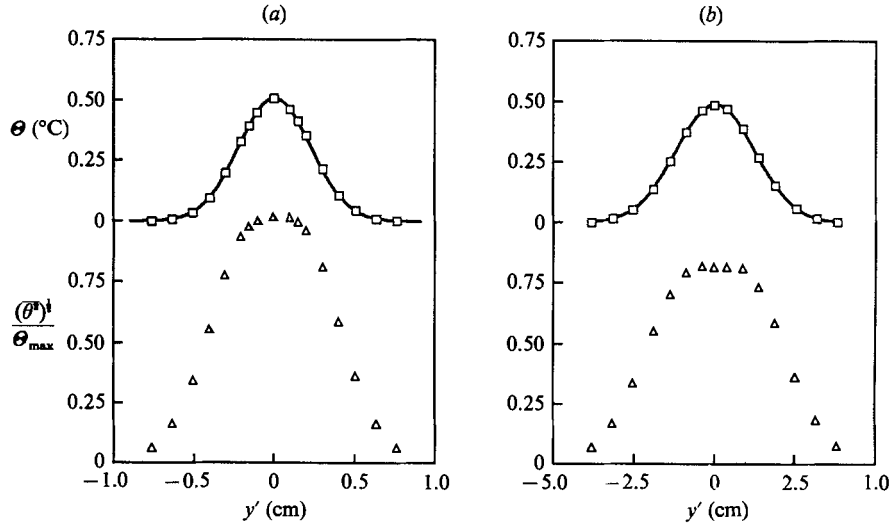

FIGURE 5. The mean (Θ) and normalized r.m.s. ($(\overline{\theta^2})^{\frac{1}{2}}/\Theta_{max}$) temperature profiles at $x_0 = 62.4$ cm, $x' = 6.4$ cm ($x'/x_0 = 0.1$), (*a*) and $x_0 = 31.5$ cm, $x' = 38$ cm ($x'/x_0 = 1.21$), (*b*). □, mean; △, r.m.s. Homogeneous biplanar grid; $M = 2.5$ cm.

5.1.1. *The temperature moments*

Figure 5(*a*, *b*) shows mean and r.m.s. temperature profiles at different non-dimensional distances (x'/x_0) from the source. The data in figure 5(*a*) were obtained with $x_0 = 62.4$ cm and $x' = 6.4$ cm, yielding a non-dimensional distance $x'/x_0 = 0.10$, while the data in figure 5(*b*) pertain to an x_0 of 31.5 cm and an x' of 38 cm yielding $x'/x_0 = 1.21$. The r.m.s. profiles have been normalized by the respective maximum mean temperatures, Θ_{max} (the same as the centreline temperature here). The source strengths were 19 W/m and 127 W/m respectively. The curves shown in the figures for the mean temperature profiles are best fit (least squares) Gaussian profiles; they represent the data extremely well. The variance profiles are single peaked, however, the peak (especially in the case of $x'/x_0 = 1.21$) is very flat indicating that the locations are close to the regions where double peaks may be observed. Double peaks are observed in the very early stages of the turbulent convective regime and in the final stages of evolution, when the instantaneous plume is comparable in width to the mean plume (Warhaft 1984; Lumley & Van Cruyningen 1985). Our data sets (see below) are not in these regions.

Anand & Pope (1983) and Warhaft (1984) showed that data obtained at various x/M and for different x_0, could be collapsed onto a single curve when plotted as $l_{\frac{1}{2}}/l_0$ *vs.* x'/x_0 for both the temperature mean and variance. Here $l_{\frac{1}{2}}$ is defined, in the usual way, as the lateral distance from the centre to a point whose ordinate is half that of the point on the centre line, and l_0 is the turbulence lengthscale defined as $(\overline{u^2})^{\frac{3}{2}}/\epsilon$ at the source. Figure 6 shows data obtained in the present study plotted alongside those of Warhaft (1984). The agreement is very good and this is not surprising for the turbulence field was generated with the same grid in both the experiments, although the mean velocities were slightly different. The normalized centreline intensity $(\overline{\theta^2_{cl}})^{\frac{1}{2}}/\Theta_{max}$ also agreed to within a few percent with the measurements of Warhaft (1984). Note that the first station lies in the middle of the turbulent-convective region while the second measurement station lies in the transition region between the

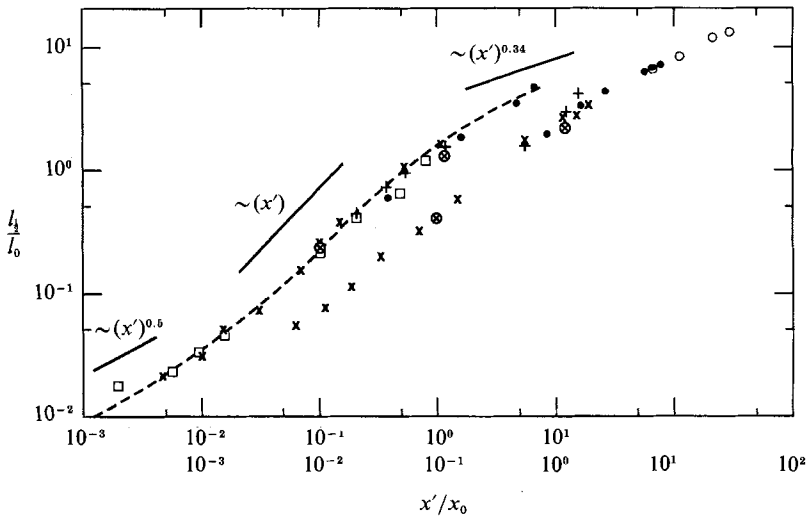

FIGURE 6. Normalized half-width of the mean temperature profiles (left-hand curve) and r.m.s. temperature profiles (right-hand curve) for the biplanar 2.5 cm grid. The open circles with the cross, ⊗, are the data for the present experiments. The other symbols are for the various source locations used by Warhaft (1984, figure 10) from which this figure is taken.

turbulent-convective and turbulent-diffusive regimes, thus the double peaks discussed above are not observed here.

5.1.2. *The temperature spectra*

One-dimensional temperature power spectra $F_{\theta\theta}(\kappa_1)$ were estimated from the time series using Taylor's frozen flow hypothesis. Spectra were obtained at various lateral positions at the two downstream locations discussed above, namely $x = 68.8$ cm, $x'/x_0 = 0.10$ and $x = 69.5$ cm, $x'/x_0 = 1.21$ and these are shown in figures 7 (*a*) and 7 (*b*) respectively. The spectra are accurate up to 2.5 kHz ($\kappa_1 \sim 2500$ m^{-1}) beyond which the sensor sensitivity begins to roll off. In grid turbulence, typically, the dissipation spectrum peaks at approximately 30η (η is the Kolmogorov microscale) and has a negligible contribution from scales smaller than 6η (see for example Warhaft & Lumley 1978). Here, since the Prandtl number is approximately 0.7 and η is 3×10^{-4} m, the bandwidth of the temperature sensor is large enough to resolve all the dynamically important scales.

The spectra shown in figure 7 (*a*, *b*) are one-sided, hence,

$$\int_0^\infty F_{\theta\theta}\,\mathrm{d}\kappa_1 = \overline{\theta^2}.$$

In each case the lateral positions have been chosen so as to span one half of the mean temperature profile ($y' = 0$ to $y' \approx -3l_{\frac{1}{2}}$). For clarity each of the spectra has been shifted down by half a decade with respect to the one above it. The spectra obtained at $x'/x_0 = 0.10$ are wider than those at $x'/x_0 = 1.21$, as expected from the smaller mean and instantaneous plume widths at $x'/x_0 = 0.10$. (The velocity field is nearly identical in both the cases.)

Figure 8 (*a*, *b*) shows plots of $\kappa_1 F_{\theta\theta}(\kappa_1)/\overline{\theta^2}$, at the same locations as in figure 7 (*a*, *b*). The spectra were fitted with a tenth-order polynomial in log–log space prior to scaling by κ_1. The origin of the ordinate has been shifted down by 0.1 successively for

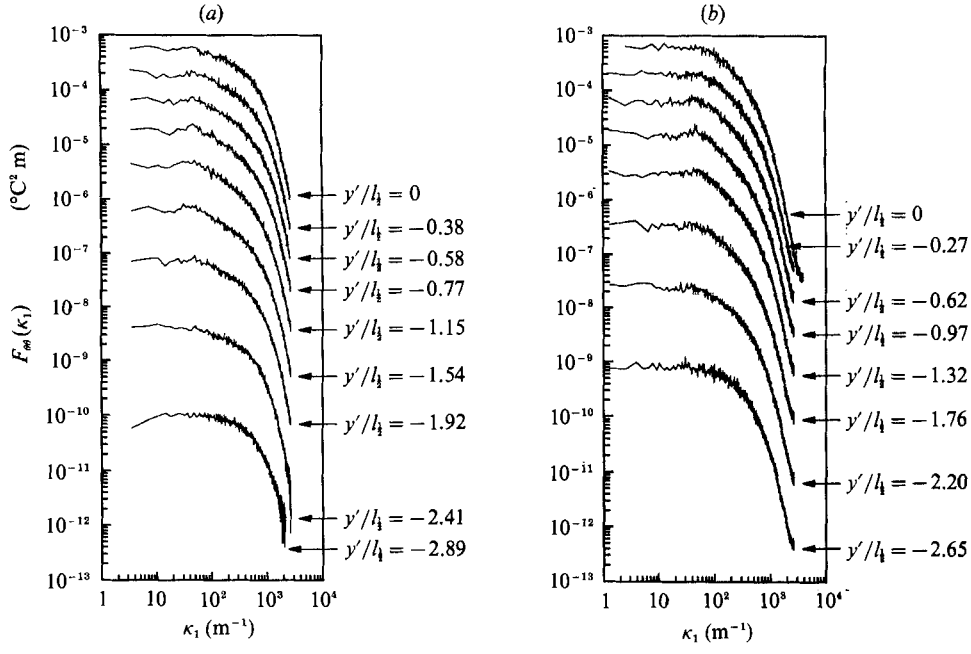

FIGURE 7. One-dimensional spectra of temperature fluctuations as a function of lateral position in the plume for the 2.5 cm biplanar homogeneous grid. (*a*) $x = 68.8$ cm, $x'/x_0 = 0.1$. (*b*) $x = 69.5$ cm, $x'/x_0 = 1.21$. The spectra span one side of the mean plume which is symmetric, their lateral position is shown on the graph. Each spectrum has been shifted down by a half a decade with respect to the one above it for clarity.

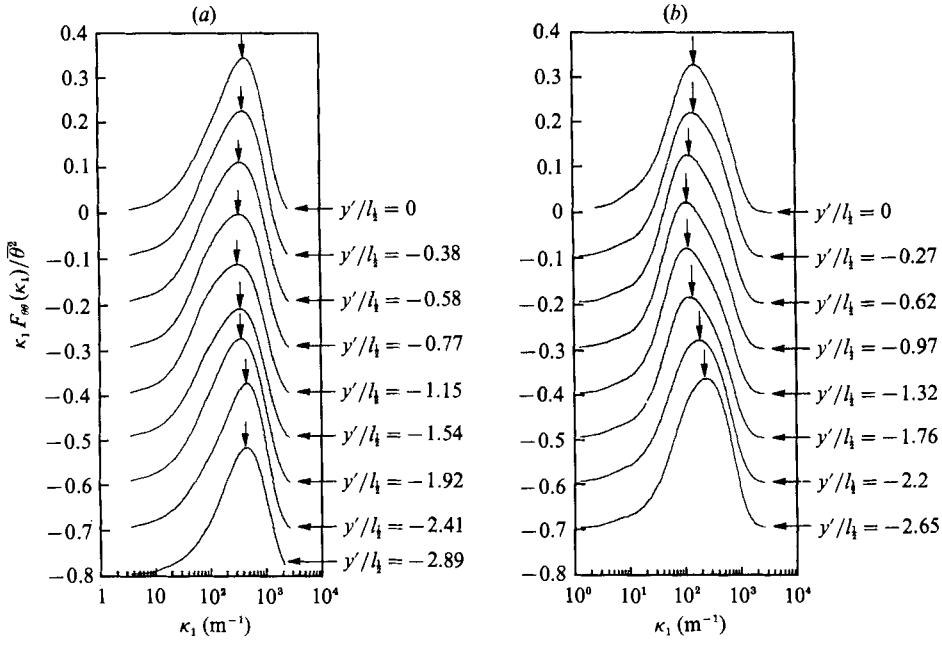

FIGURE 8. The normalized temperature spectra of figure 7 multiplied by κ_1. The arrows indicate the location of the peaks. For clarity the origin of the ordinate has been shifted down by 0.1 successively. (*a*) $x'/x_0 = 0.1$; (*b*) $x'/x_0 = 1.21$.

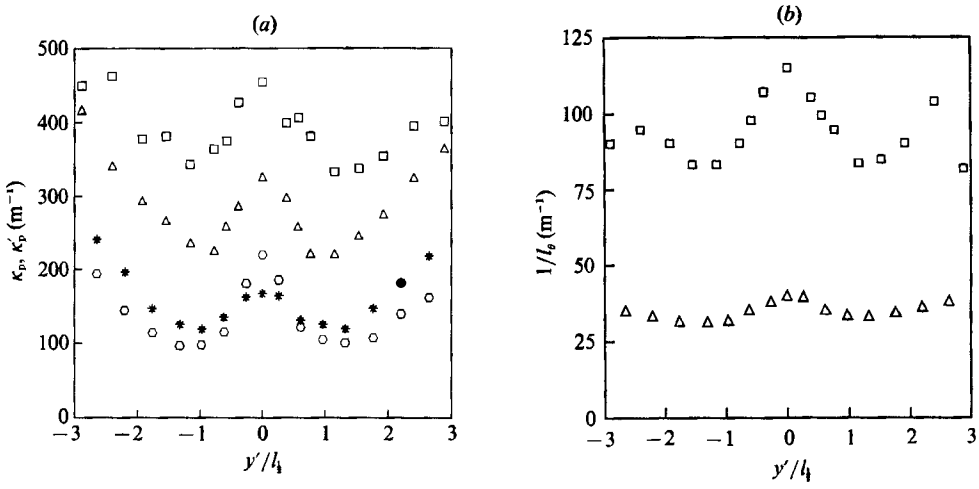

FIGURE 9. (*a*) The wavenumber at which the temperature spectra peak as a function of lateral distance across the plume for the homogeneous bi-planar grid. The peaks of the unconditioned spectra are taken from figure 8. □, unconditioned spectrum at $x'/x_0 = 0.1$; △, conditioned (or intermittency) spectrum at $x'/x_0 = 0.1$; *, unconditioned spectrum at $x'/x_0 = 1.21$; ○, conditioned spectrum at $x'/x_0 = 1.21$. (*b*) The (inverse) integral lengthscale (l_θ^{-1}) across the plume determined from the relation $\epsilon_\theta/((\overline{u^2})^{\frac{1}{2}}\overline{\theta^2})$; □, $x'/x_0 = 0.1$; △, $x'/x_0 = 1.21$. The lateral distance y' in both (*a*) and (*b*) has been normalized by the plume half-width.

clarity. The arrows shown in the figures mark the locations of the peaks of the spectra. The peak wavenumber, κ_p, may be viewed as an approximate measure of the inverse of the thermal lengthscale l_θ. Proceeding from the centre to the edge of the plume, the location of the peak is seen first to shift to lower wavenumbers and then rise once more, at both values of x'/x_0. The locations of the peaks of the spectra in figure 8(*a*, *b*) are shown in figure 9(*a*). (The figure uses data spanning the full mean plume and not just one half.) Also shown in the figure are similar peaks obtained from the spectrum of the intermittency function, $F_\Gamma(\kappa_1)$. The intermittency function $\Gamma(t)$, was obtained from the time series by assigning a value of 1 to points with an instantaneous temperature excess (over the ambient temperature) greater than $4\sigma_n$. (σ_n is the r.m.s. of noise fluctuations, obtained from measurements in cold air.) As pointed out by Chatwin & Sullivan (1989), such a definition for $\Gamma(t)$ is not rigorous and quantitative information obtained therefrom should be treated with caution as it is very sensitive to the choice of the threshold (in this case $4\sigma_n$), however, given the qualitative nature of the discussion to follow, it is quite adequate.

At the centre (of the mean plume) the instantaneous plume is present most of the time, while, at the edge (of the mean plume) the instantaneous plume is absent most of the time. Hence in both these regions the intermittency function undergoes rapid changes of the type one-zero-one at the centre and zero-one-zero near the edge. Thus, the $\kappa_1 F_\Gamma(\kappa_1)$ spectrum has a high wavenumber peak arising from these rapid changes. In the intermediate region the instantaneous plume is present or absent for more equal lengths of time and transitions in $\Gamma(t)$ are not so rapid, hence the peak of $\kappa_1 F_\Gamma(\kappa_1)$, κ_p', shifts to lower wavenumbers. Thus κ_p' behaves as shown in figure 9(*a*).

Variations in temperature observed at any position, arise from the internal structure and jiggling (small excursions of high frequency caused by the fine-scale structure of the velocity field) of the instantaneous plume and from the flapping motion caused by the large-scale velocity fluctuations. Hence the overall spectrum

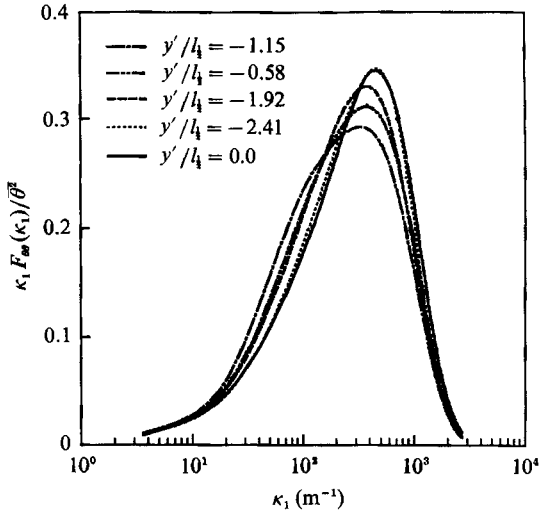

FIGURE 10. An attempt to collapse the data of figure 8(*a*).

may be viewed as a convolution of the 'plume' spectrum and the 'flapping' spectrum, $F_I(\kappa_1)$ (cf. Fackrell & Robins 1982). For $x'/x_0 = 0.10$ we see that the behaviour of κ_p closely mimics that of κ'_p, though it occurs at much larger wavenumbers, because the instantaneous plume width is small compared to the convective lengthscale ($\sigma_p/(\overline{v^2})^{\frac{1}{2}}t \approx 0.4$, σ_p is the standard deviation of the Gaussian distribution representing the instantaneous plume). The correspondence is less pronounced for the data at $x'/x_0 = 1.21$. For this case, in the central region of the mean plume, the intermittency function suggests that κ_p should occur at much higher wavenumbers than observed. The reason for this anomaly is that the temperature signal here exhibits intermittency due to both bulk flapping of the plume and due to the presence of pockets of cold air in the instantaneous plume. At $x'/x_0 = 0.10$, the instantaneous plume has very little internal structure and hence the intermittency arises due to flapping only. Further downstream, when the plume is in the turbulent diffusive phase, flapping ceases to play a role in the central region of the mean plume and thus the peak wavenumber of the overall spectrum should become independent of lateral position in this region, which is consistent with the behaviour exhibited by the data in figure 9(*a*). It is unclear, however, why the conditioned profile still shows a sharp peak in the centre.

Figure 9(*b*) shows the inverse thermal lengthscale l_θ^{-1} determined as $\epsilon_\theta/(\overline{u^2})^{\frac{1}{2}}\overline{\theta^2}$, plotted as a function of $y'/l_{\frac{1}{2}}$, at $x'/x_0 = 0.10$ and $x'/x_0 = 1.21$. The data have the same qualitative features as the plots of κ_p, the inverse thermal lengthscale determined from the spectrum, shown in figure 9(*a*). Thus there is a peak at the centre and a minimum on either side of the centre which occurs at approximately the same location as in figure 9(*a*). However, for $x'/x_0 = 1.21$, the overall variation of l_θ^{-1} (figure 9*b*) is less than that of κ_p (figure 9*a*) and the peak at the centre is relatively broader. This difference may be due to the fact that the form of the spectrum changes as the plume is traversed (i.e. they are not self-similar, as is discussed in the next paragraph) and thus the peak of the spectrum is not a perfectly conditioned estimate of the thermal lengthscale. Nevertheless the correspondence between κ_p and l_θ^{-1} is remarkably good.

Figure 10 shows an attempt to collapse the data in figure 8(*a*). The lack of

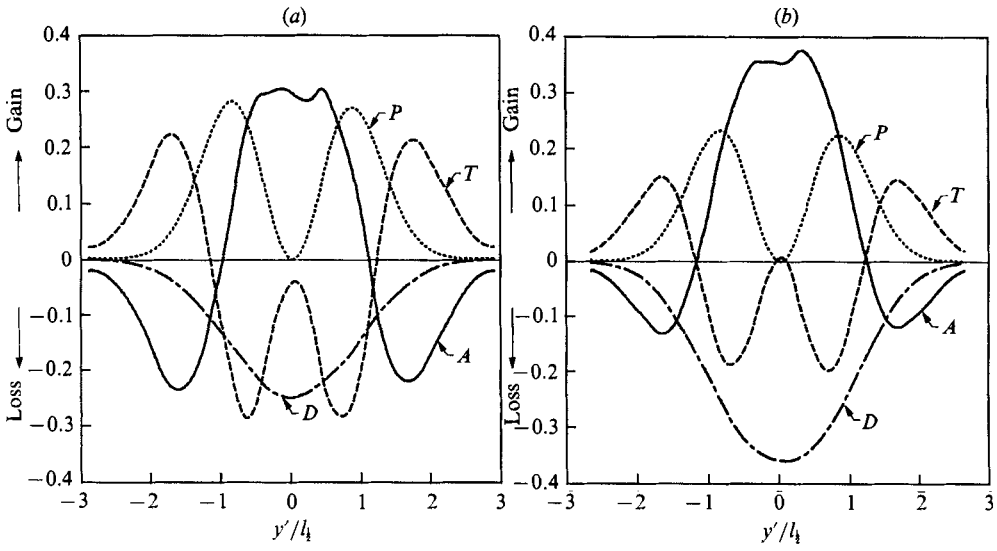

FIGURE 11. The temperature variance budget (equation (6)) for the line source in the homogeneous grid turbulence. The ordinate values have been normalized by $(\Theta^2_{\max} U)/x'$. The labels indicated in the figure are: A, normalized advection; P, normalized production; T, normalized transport and D, normalized destruction. (*a*) $x'/x_0 = 0.10$; $x_0 = 62.4$ cm. (*b*) $x'/x_0 = 1.21$, $x_0 = 31.5$ cm.

similarity mentioned above between the spectra at different lateral positions is clearly evident in these figures. Proceeding from the centre to the edge we see first a tendency for the low wavenumber region to be relatively enhanced, however, further away the spectra revert to that at the centreline; the spectrum obtained at $y' = -2.41 l_{\frac{1}{2}}$ collapses well onto the centreline spectrum. As mentioned above, the overall spectrum may be viewed as a convolution of the 'plume' spectrum and the 'flapping spectrum'. Hence, since the 'flapping' spectrum is similar in the centre and the edge of the mean plume, the overall spectra are similar in these regions too. A similar comparison for the data in figure 8(*b*) (not shown) indicates that the spectra at the edge do not resemble the centreline spectrum as well. The dependence of the spectra on the lateral coordinate y', is examined in greater detail in the discussion for the inhomogeneous turbulence field below.

5.1.3. *The temperature variance budget*

The temperature variance budget (equation (6)) has been discussed in §2. Figure 11(*a*, *b*) shows a balance between various terms described in equation (6) obtained at $x'/x_0 = 0.10$ and $x'/x_0 = 1.21$, respectively. The ordinates of the curves have been normalized by $\Theta^2_{\max} U/x'$ and the abscissae have been non-dimensionalized by $l_{\frac{1}{2}}$.

The production and transport terms were obtained by fairing a smooth curve through the data points (data for Θ, $\overline{\theta v}$, and $\overline{\theta^2 v}$) using Bezier splines, prior to numerical differentiation using a 5-point window. No symmetry condition was imposed on the curve-fit and it is quite reassuring that the curves exhibit a high degree of symmetry about the origin. The destruction term, ϵ_θ, was obtained by two different methods. In the first method ϵ_θ was obtained by differentiating the time series and invoking local isotropy and Taylor's frozen flow hypothesis, i.e.

$$\epsilon_\theta = \frac{-3\alpha}{U^2} \overline{\frac{\partial\theta}{\partial t} \frac{\partial\theta}{\partial t}}.$$

Equivalently, ϵ_θ was evaluated from the one-sided temperature spectrum $F_{\theta\theta}(\kappa_1)$ as

$$-12\pi^2\alpha \int_0^\infty \kappa_1^2 F_{\theta\theta}\, \mathrm{d}\kappa_1$$

(a seventh-order polynomial was fit to the spectra in log–log space prior to integration). In both cases the contribution from background noise was subtracted out on a mean-square basis. The two methods agreed to within 10%, however, the values of ϵ_θ shown in figure 11(*a*, *b*) were obtained by the spectral method. Differentiation via spectra is more accurate and furthermore it is possible to extend the curves fit to the spectra to wavenumbers beyond the high-frequency cut-off of the temperature sensor and thus it is possible to partly account for the unresolved scales (this resulted in approximately a 3% increase in the estimate for ϵ_θ). The advection term was not measured but obtained as the difference of the other terms in the budget. The accuracy of such a method of obtaining the advection term is discussed in Appendix A.

We see from figure 11(*a*) that in the central region of the plume, the production and transport terms are approximately equal in magnitude (but opposite in sign), while advection balances destruction. At the outer edges of the plume, however, the production and destruction terms rapidly approach zero and advection and transport balance each other.

The curves shown in figure 11(*b*) show the same qualitative behaviour as those in figure 11(*a*). Here, too, the advection term balances the destruction term in the central region of the plume while it balances the transport term in the outer regions. However, the relative importance of the terms viewed across the whole plume is very different. The peaks of the non-dimensional production and transport terms are lower at $x'/x_0 = 1.21$ when compared with those at $x'/x_0 = 0.10$, while the peak of the destruction term is larger by approximately 50%. Hence, while the peaks of all four terms are approximately equal at $x'/x_0 = 0.10$, the destruction peak (and hence the advection peak) is almost twice as large as those of the production and transport peaks, at $x'/x_0 = 1.21$.

We note that when $x'/x_0 = 0.10$, the plume is at the centre of the turbulent-convective regime, while, when $x'/x_0 = 1.21$, it is in the transition region between the turbulent-convective and turbulent-diffusive phases (figure 6). Mixing is most vigorous in the turbulent-convective region, evidenced by the rapid growth of the half-width in this regime, hence the transport term diminishes in importance when x'/x_0 is increased from 0.10 to 1.21. For the same reason the relative magnitude of the heat flux $\overline{\theta v}$ decreases, however, the change in the production term is not so pronounced because the mean temperature gradient remains unchanged with our choice of scaling parameters. The destruction term (and consequently the advection term) shows by far the greatest change and this can be understood as follows. Close to the source, the instantaneous plume has very little internal structure since there is little turbulent activity in scales smaller than the plume width and hence the major contribution to the destruction term comes from the edge regions of the instantaneous plume where the temperature gradients are large. Further away from the source the plume develops internal structure and patches of cold fluid are interspersed with hot patches (Stapountzis *et al.* 1986). Hence the volume over which large gradients exist, increases with distance from the source, resulting in a larger non-dimensional destruction term.

The measurements presented here are in rough qualitative agreement with those

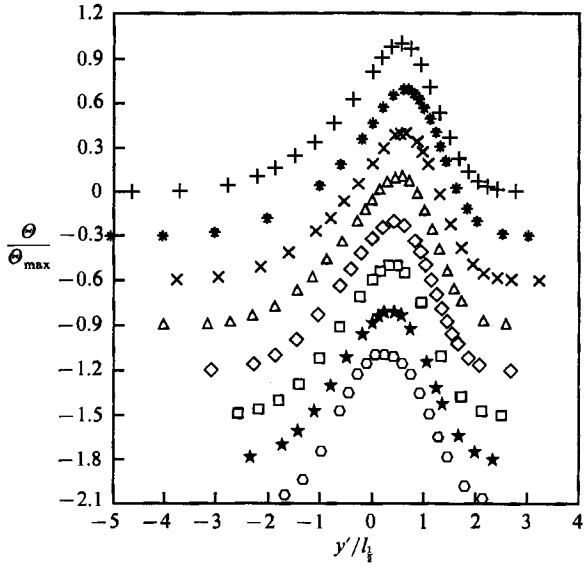

FIGURE 12. The mean temperature profiles for the plume in the 3.3:1 inhomogeneous, parallel bar grid mixing layer. The mean temperature has been normalized by the temperature maximum at that downstream location. The profiles are plotted with respect to y_0 and the abscissa is normalized by the plume half width (table 2). The heated wire is at $x_0 = 31.5$ cm ($10M_2$). The symbols for the downstream measuring stations x'/x_0, are +, 0.05; *, 0.1; ×, 0.202; △, 0.4; ◇, 0.603; □, 0.848; ☆, 1.21; ○, 2.91. For measurements up to $x'/x_0 = 0.4$ the 0.076 mm diameter wire was used (29.5 W/m), beyond that the 0.127 mm diameter wire (127 W/m) was used.

of Freymuth & Uberoi (1971) for flow around a heated cylinder and Freymuth & Uberoi (1973) for flow around a heated sphere. In those experiments too, advection balanced destruction in the central region of the thermal field, while it balanced transport in the outer regions. However, the details of the budget are quite different from those presented here because the velocity fields are dissimilar.

5.2. *Dispersion from the line source in the inhomogeneous velocity field*

As discussed in §5.1, the development of the thermal plume consists of three stages: (*a*) molecular diffusive; (*b*) turbulent convective and (*c*) turbulent diffusive. The development of the plume in the molecular diffusion phase is identical in both homogeneous and inhomogeneous turbulence fields. Thus no attempt was made here to duplicate the results of Warhaft (1984) where this regime was studied in some detail for a homogeneous velocity field. The measurements of the thermal field here span the entire turbulent-convective range, however, because of the growth of the boundary layers on the tunnel walls and the development of irregularities in the velocity field (VW), they could be extended only to the beginning of the turbulent diffusive range. Unless otherwise specified, for the thermal field described below, the inhomogeneous turbulence field was generated using the 3.3:1 parallel bar grid.

5.2.1. *The moments of the temperature field*

Mean temperature profiles obtained at various distances from the source are shown in figure 12 ($x_0 = 31.5$ cm, $y_0 = 17.53$ cm). The curves have been normalized by their respective peak mean temperature, Θ_{max}, while the lateral spread has been centred about the location of the line source, y_0, and normalized by the half width $l_{\frac{1}{2}}$. In a manner analogous to that for symmetric profiles, the half width has been defined as

x' (cm)	$\frac{x'}{x_0}$	Θ_{max} (°C)	Y_p (cm)	Y_c (cm)	$l_{\frac{1}{2}}$ (cm)	$l^+_{0.5}$ (cm)	$l^-_{0.5}$ (cm)	$l^-_{0.5}/l^+_{0.5}$	$l^+_{0.2}$ (cm)	$l^-_{0.2}$ (cm)	$l^-_{0.2}/l^+_{0.2}$	$(\overline{\theta^2_{max}})^{\frac{1}{2}}$ (°C)	$\frac{(\overline{\theta^2_{max}})^{\frac{1}{2}}}{\Theta_{max}}$	$l'^+_{0.5}$	$l'^-_{0.5}$ (cm)	$l'^-_{0.5}/l'^+_{0.5}$ (cm)
1.6	0.05	1.41	0.08	0.01	0.14	0.11	0.17	1.53	0.16	0.30	1.9	1.45	1.03	0.10	0.23	2.35
3.15	0.10	0.73	0.17	0.04	0.25	0.19	0.31	1.61	0.29	0.56	1.97	0.87	1.19	0.20	0.35	1.75
6.35	0.20	0.37	0.29	0.08	0.47	0.36	0.59	1.65	0.53	1.03	1.94	0.49	1.33	0.33	0.65	1.97
12.6	0.40	0.19	0.49	0.11	0.88	0.65	1.12	1.72	0.96	1.84	1.92	0.27	1.37	0.62	1.05	1.69
19.0	0.60	0.64	0.55	0.16	1.23	0.99	1.47	1.49	1.44	2.36	1.64	0.80	1.24	0.86	1.56	1.83
26.7	0.85	0.45	0.63	0.21	1.62	1.34	1.90	1.42	1.95	2.95	1.51	0.54	1.20	1.13	2.10	1.85
38.0	1.21	0.36	0.75	0.29	2.06	1.74	2.39	1.37	2.54	3.61	1.42	0.41	1.15	—	—	—
91.8	2.91	0.15	0.89	0.78	3.69	3.62	3.76	1.04	5.08	5.37	1.06	0.16	1.05	—	—	—

TABLE 2. Evolution of the line source in the inhomogeneous velocity field generated by the 3.3:1 bar grid. The symbols Y_p, Y_c, $l^-_{0.5}$, etc. are described in §5.2.1. $x_0 = 31.5$ cm; $y_0 = 17.53$ cm. The first four measurements ($x' = 1.6$, 3.15, 6.35 and 12.6 cm) are for the low heating (0.076 mm diameter wire operated at 29.5 W/m); the final four downstream measurements are for the high heating (0.127 mm diameter wire operated at 127 W/m). The lengthscales $l'^+_{0.5}$ and $l'^-_{0.5}$ are not reported for the last two downstream stations as the variance profiles exhibited double peaks there.

half the separation between points at a mean temperature equal to $0.5\Theta_{max}$. The values of Θ_{max} and $l_{\frac{1}{2}}$ for various x'/x_0 are documented in table 2. For the measurements up to $x'/x_0 = 0.4$, the 0.076 mm diameter wire, at a strength of 29.5 W/m was used to generate the thermal source while, beyond $x'/x_0 = 0.4$, the 0.127 mm diameter wire at a strength of 127 W/m was used.

We note that close to the source the profiles are highly asymmetric with a larger spread on the small-scale side and a smaller spread on the large-scale side. Far away from the source (the largest x'/x_0 shown), however, the profile is nearly symmetric about the peak. Close to the source (but beyond the molecular diffusive regime), spreading is primarily due to the flapping of the instantaneous plume by the fluctuating transverse velocity, v. As shown in §4 (see also VW), the v fluctuations in the mixing layer are highly skewed, with fluctuations originating from the large-scale homogeneous region of the mixing layer being predominantly negative, and fluctuations originating from the small-scale homogeneous region being predominantly positive. Hence, large excursions of the instantaneous plume from its mean location, caused by the large-scale fluctuations, are directed towards the small-scale region and conversely, the excursions towards the large-scale region are much smaller. Consequently, the mean temperature profile has a larger spread on the small-scale side than on the large-scale side. Owing to this asymmetric mixing the maximum and median temperature locations are deflected into the region of $y' > 0$ (see also Hunt 1985) and the magnitude of this deflection increases with x' within the turbulent-convective regime. (Note, however, that $l_{\frac{1}{2}}$ increases also and thus, in figure 12, the peak temperature location appears to move closer to the origin y_0 as x' increases.) When the width of the mean plume becomes comparable with the turbulence integral lengthscale, turbulent diffusion begins to play a role in the mixing and the plume starts to spread faster on the large-scale side because of the larger eddy diffusivity there. At $x'/x_0 = 2.91$ the two effects are approximately in balance and the mean temperature is nearly symmetric. Beyond this location, when turbulent diffusion becomes the dominant spreading mechanism one would expect to see asymmetric profiles once more but with a larger spread on the large-scale side of the mixing layer.

Figure 13(*a*) shows iso-fraction lines (i.e. loci of points satisfying $\Theta/\Theta_{max} =$ const.), obtained from the data presented in figure 12. The transverse motion of the peak temperature has been subtracted out in this figure. We note that although the data were obtained from sources of two different strengths and initial sizes, the curves are smooth and match well at $x'/x_0 = 0.4$ where the thermal field produced by the small intensity source is replaced by that of the higher intensity source (§2). A similar procedure was used by Warhaft (1984).

The asymmetry of the mean temperature profiles close to the source and the tendency towards symmetry far away from it are clearly evident in this figure. Extrapolation of the iso-fraction lines beyond the measurement region suggests that the mean temperature profiles would indeed become asymmetric once again, with a larger spread on the large-scale side, as expected. Let us define the one-sided half-widths as follows:

$l^+_{0.5} \equiv$ distance from the peak to a point at $0.5\Theta_{max}$, lying to the right of the peak;
$l^-_{0.5} \equiv$ distance from the peak to a point at $0.5\Theta_{max}$, lying to the left of the peak.

Similarly,

$l^+_{0.2} \equiv$ distance from the peak to a point at $0.2\Theta_{max}$, lying to the right of the peak;
$l^-_{0.2} \equiv$ distance from the peak to a point at $0.2\Theta_{max}$, lying to the left of the peak.

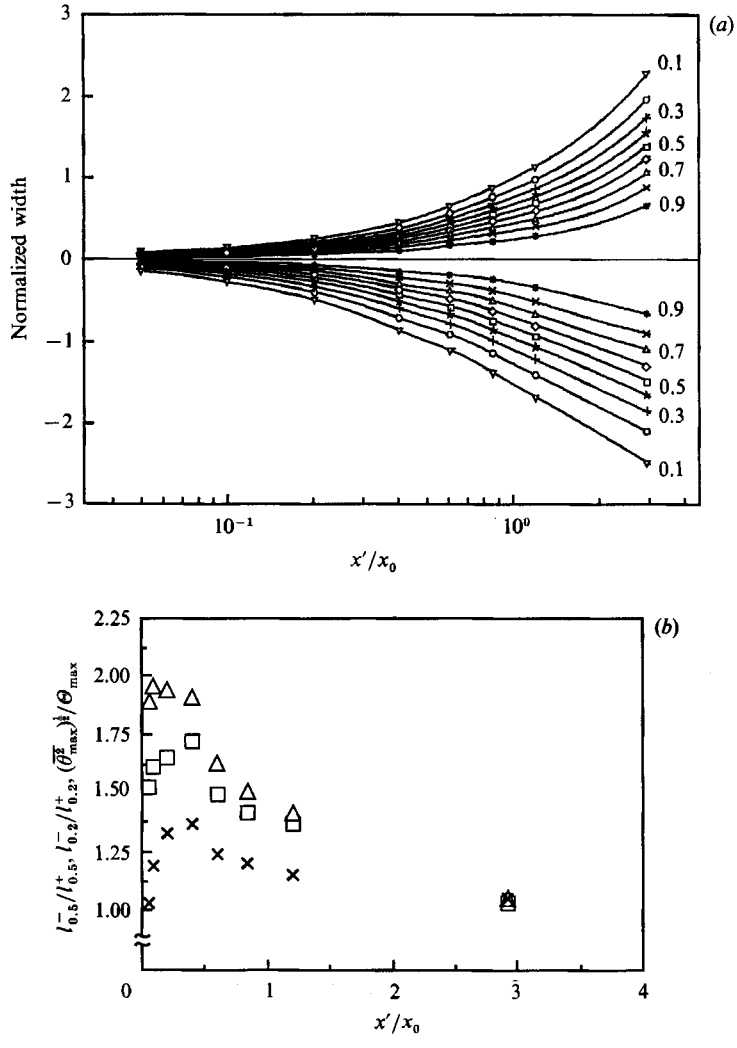

FIGURE 13. (*a*) Iso-fraction lines (Θ/Θ_{max} = const.) for the profiles of figure 12. The transverse motion of the peak has been subtracted out. The ordinate has been normalized by the large-scale turbulence integral lengthscale at the source (table 1). The labels (0.1, 0.3, etc.) refer to the fraction value with respect to the peak. (*b*) Variation of the asymmetry parameters (see text and table 2) □, $l_{0.5}^-/l_{0.5}^+$; △, $l_{0.2}^-/l_{0.2}^+$; ×, the ratio of the peak r.m.s. temperature to the mean temperature maximum. Grid and source location for (*a*) and (*b*) are the same as in figure 12.

The ratios $l_{0.5}^-/l_{0.5}^+$ and $l_{0.2}^-/l_{0.2}^+$ could then be used to quantify the asymmetry of the mean temperature profiles. The downstream evolution of these ratios is shown in figure 13(*b*). We note that when the ratios are larger than unity, $l_{0.2}^-/l_{0.2}^+$ is always larger than $l_{0.5}^-/l_{0.5}^+$. Both the profiles show a region of growth (both ratios should be unity initially) and then decay to a value of 1 at the end of the turbulent convective regime. As reported in table 2, the peak value of $l_{0.5}^-/l_{0.5}^+$ is approximately 1.7, while that of $l_{0.2}^-/l_{0.2}^+$ is close to 2. The data suggest that the approach to unity at large x'/x_0 is not asymptotic indicating that the ratios would be less than unity in the turbulent diffusive range as discussed above.

Temperature variance, $\overline{\theta^2}$, profiles obtained at various downstream locations are

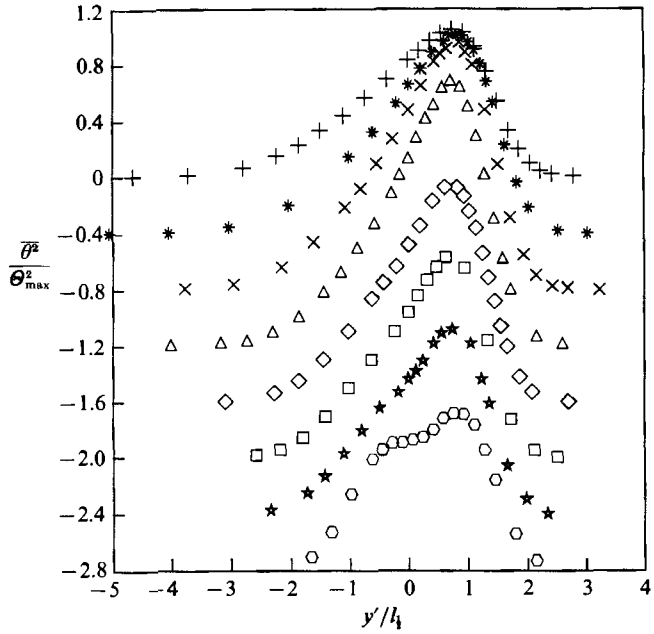

FIGURE 14. Temperature variance profiles for the 3.3:1 bar grid with source at $x_0 = 31.5$ cm. Symbols are for the same locations as figure 12.

shown in figure 14. $\Theta_{\max}$ and $l_{\frac{1}{2}}$ obtained from the mean temperature data, have been used to normalize these curves also. The asymmetry is even more marked here than in the Θ profiles (figure 12) and the tendency towards symmetry is slower. We could define one-sided half-widths for the variance profiles, $l'^{+}_{0.5}$ and $l'^{-}_{0.5}$ in the same way as $l^{+}_{0.5}$ and $l^{-}_{0.5}$ above. Table 2 documents the ratios $l'^{-}_{0,5}/l'^{+}_{0.5}$ at various x'/x_0. The peak value of $l'^{-}_{0,5}/l'^{+}_{0.5}$ is approximately 2.35. The ratio is not properly defined at large x'/x_0 since the variance profiles begin to exhibit double peaks. As mentioned in §5.1, double peaks are expected in the variance profiles far from the source when the width of the instantaneous plume becomes large compared to the flapping lengthscale (Warhaft 1984; Lumley & Van Cruyningen 1985).

Figure 13(*b*) also shows the development of the ratio $(\overline{\theta^2_{\max}})^{\frac{1}{2}}/\Theta_{\max}$. Its peak value is approximately 1.4 in the region close to the source and it asymptotes to a value of approximately 1.0. This behaviour is consistent with that observed by Warhaft (1984).

The evolution of the half widths of the Θ and $\overline{\theta^2}$ profiles is shown in figure 15(*a*). The half widths have been normalized by l_{02}, the integral lengthscale of the high turbulence region, obtained at x_0. Both the half widths display a nearly linear growth ($x^{0.83}$ and $x^{0.82}$ respectively) indicating that the plume is in the turbulent-convective regime.

Figure 15(*b*) shows the evolution of the location of the mean temperature peak, Y_p, and the location of the centre of mass of the mean temperature profile

$$Y_c \left(\equiv \int_{-\infty}^{\infty} \Theta y \, dy \Big/ \int_{-\infty}^{\infty} \Theta \, dy \right).$$

For a symmetric profile Y_p should equal Y_c, and the greater the difference between Y_p and Y_c, the greater the asymmetry. In addition, it can be shown that when flapping

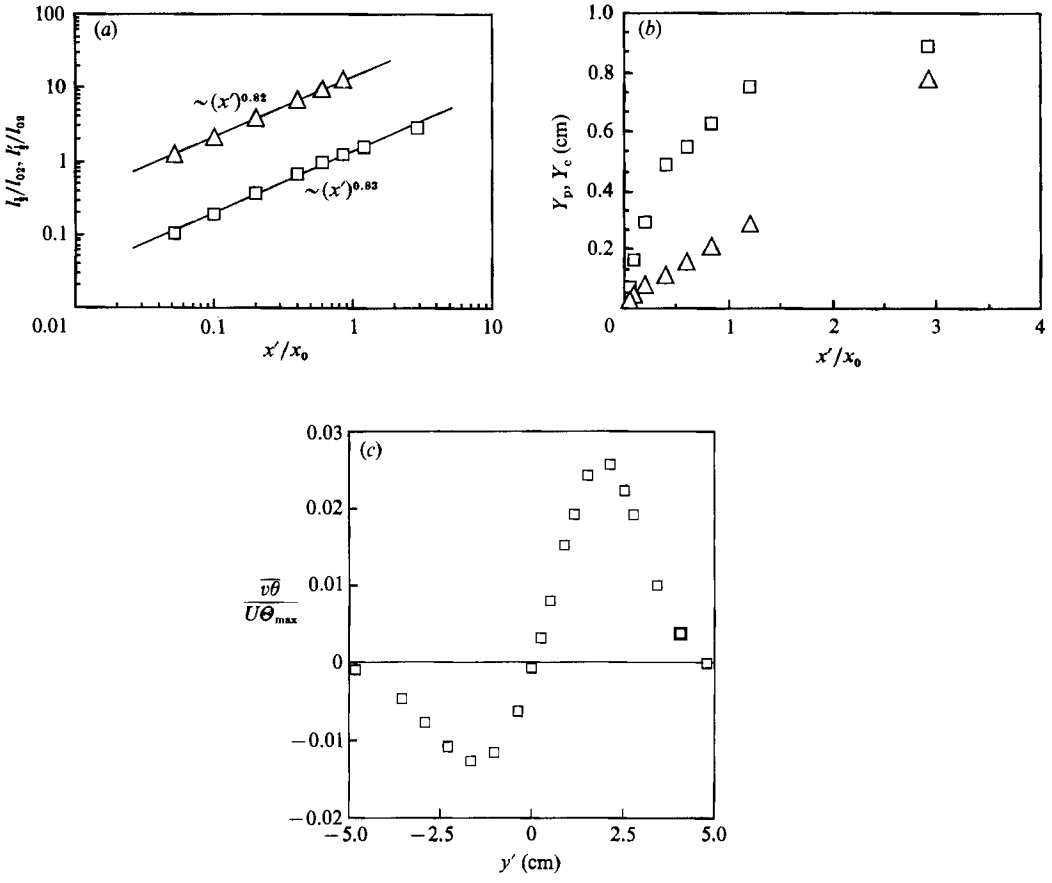

FIGURE 15. (*a*) Evolution of the half width of the mean (□) and variance (△) of the temperature profiles normalized by $l_{0\theta}$, the integral lengthscale of the high-turbulence region obtained at the source. (The graph of the variance has been shifted up a decade for clarity.) (*b*) Evolution of the transverse location of the mean temperature peak, Y_p, □, and centre of mass, Y_c, (median) of the mean temperature profile △, for the profiles of figures 12. (*c*) Normalized transverse heat flux as a function of y at $x'/x_0 = 1.21$.

is the sole mixing mechanism, $\mathrm{d}Y_c/\mathrm{d}x$ must be zero if the instantaneous plume is symmetric about its peak. The transport equation for Y_c is given by equation (5) (§2). An examination of the data at $x'/x_0 = 0.85$ and $x'/x_0 = 1.21$ shows that the integral of the $\overline{v\theta}$ profile (figure 15*c*) is non-zero and thus indicates a positive value for $\mathrm{d}Y_c/\mathrm{d}x$ and accounts for approximately 60% of its magnitude. At both these locations $\mathrm{d}Y_c/\mathrm{d}x$ is approximately 1.1×10^{-2} while the term on the right-hand side of equation (5) is approximately 7.1×10^{-3} at $x'/x_0 = 0.85$ and 6.5×10^{-3} at $x'/x_0 = 1.21$.

5.2.2. *The temperature spectra*

Figure 16(*a*, *b*) shows normalized one-dimensional temperature power spectra $F_{\theta\theta}(\kappa_1)/\overline{\theta^2}$ for the 3.3:1 bar grid, obtained at $x'/x_0 = 0.10$ ($x_0 = 68.4$ cm) and at $x'/x_0 = 1.12$ ($x_0 = 31.5$ cm) respectively. For clarity each spectrum has been shifted down by a decade with respect to the one above it. The spectra obtained at $x'/x_0 = 0.10$ are broader than those at $x'/x_0 = 1.12$ because the mean and instantaneous plume widths are smaller close to the source (cf. §5.1.2). At both

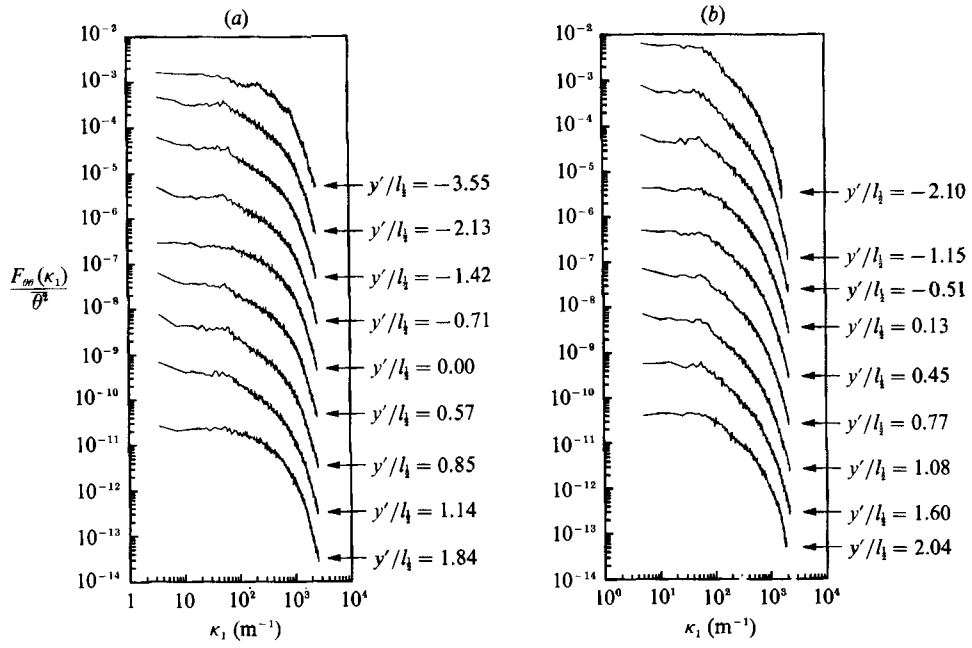

FIGURE 16. Normalized one-dimensional temperature spectra as a function of lateral position for the 3.3:1 parallel bar grid. Each spectrum has been shifted down by a decade with respect to the one above it for clarity. (*a*) $x_0 = 62.4$ cm, $x'/x_0 = 0.10$ and (*b*) $x_0 = 31.5$ cm $x'/x_0 = 1.12$.

downstream locations, proceeding from one edge of the mean plume to the other, the spectra are first seen to develop a low wavenumber hump, which disappears near the central region, reappears again and is absent once more at the other edge. This behaviour is similar to that observed for the line source in homogeneous turbulence (§5.1.2). Figure 17 (*a*, *b*) shows plots of $\kappa_1 F_{\theta\theta}(\kappa_1)/\overline{\theta^2}$ for the same data as figure 16. Each spectrum in figure 17 (*a*) has been shifted down by 0.15 with respect to the one above it, while, in figure 17 (*b*) the separation between the spectra is 0.1. The arrows in these figures denote the locations of the peaks of the spectra, κ_p. The spectra obtained at $x'/x_0 = 0.10$ show significant variation as a function of y'. The changes seen here are much more marked than the corresponding changes observed in homogeneous turbulence (figure 8*a*, *b*) because of the larger $\overline{v^2}$ and thus more vigorous mixing. The spectra clearly show two scales, one arising from flapping and the other from the jiggling motion (small excursions of high frequency) and the internal structure of the instantaneous plume. Close to the source ($x'/x_0 = 0.10$, figure 17*a*), when the instantaneous plume is thin compared to the convective lengthscales ($\sigma_p/(\overline{v^2})^{\frac{1}{2}}t \approx 0.2$, σ_p is the standard deviation of the Gaussian distribution representing the instantaneous plume), the flapping motion causes a hump to appear in the low wavenumber region of the spectra. However at the centre and edges of the plume the flapping spectrum peak shifts to higher wavenumbers because of the rapid one-zero-one and zero-one-zero changes described in §5.1.2 and thus the low wavenumber hump is absent in the overall spectra in these regions, i.e. the flapping and jiggling (and internal structure) frequencies overlap. At $x'/x_0 = 1.12$ (figure 17*b*), the width of the instantaneous plume is comparable to the convective lengthscales, thus the separation between the peaks caused by flapping and internal structure and jiggling is not large and these effects combine to give rise to single peaked spectra

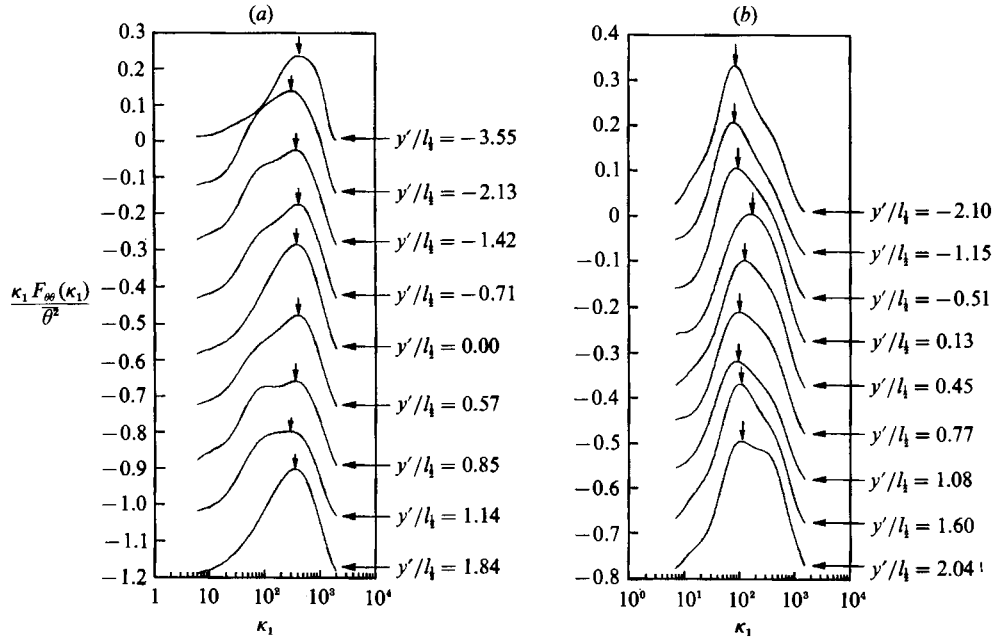

FIGURE 17. The normalized temperature spectra of figure 16 multiplied by κ_1. The arrows indicate the location of the peaks. For clarity the origin of the ordinate has been shifted down by 0.15 successively at (*a*) $x'/x_0 = 0.10$ and by 0.1 at (*b*) $x'/x_0 = 1.12$.

although there is some broadening (in this case at the edge of the plume) due to separation of the plume and flapping frequencies. (The effects described here should also be present for the dispersion of the line source in homogeneous turbulence. Figure 8 shows, however, that they are not so pronounced there.) Since the mean transverse velocity V is zero, on an average the instantaneous plume does not move from the origin, hence, in spite of the asymmetry of the velocity field, one can find corresponding points in the regions $y' < 0$ and $y' > 0$ where the normalized temperature spectra are nearly identical.

The behaviour of the peak wavenumber of $\kappa_1 F_{\theta\theta}(\kappa_1)/\overline{\theta^2}$, κ_p, across the plume, obtained from the spectra in figure 17 (*a*, *b*) is shown in figure 18 (*a*). Also shown in the figure are corresponding peak wavenumbers, κ_p', of the spectra of the intermittency function, $\kappa_1 F_\Gamma(\kappa_1)$. As mentioned in §5.1.2, the intermittency function was obtained using $4\sigma_n$ as the threshold.

All the profiles (figure 18*a*) show a central peak with troughs on either side, the reasons being the same as those outlined in §5.1.2. The profiles of κ_p and κ_p' at $x'/x_0 = 0.10$ agree with each other in the sense that the peaks and troughs occur at nearly the same lateral positions. However, other qualitative features are quite different. The profile of κ_p' is nearly a square wave while that of κ_p varies more smoothly with y'. It is unclear why this difference exists but we note that the same behaviour is seen for the 8.9:1 bar grid (figure 18*b*). The peak of the intermittency function spectrum, κ_p' lies well below κ_p across the whole plume because at $x'/x_0 = 0.10$, the convective lengthscales are much larger than the width of the instantaneous plume ($\sigma_p/(\overline{v^2})^{\frac{1}{2}}t \approx 0.2$), just as for the homogeneous velocity field case (figure 9*a*). Although the turbulent lengthscales are different in the two homogeneous edges of the mixing layer, the change in the magnitude of κ_p' is the same on either side

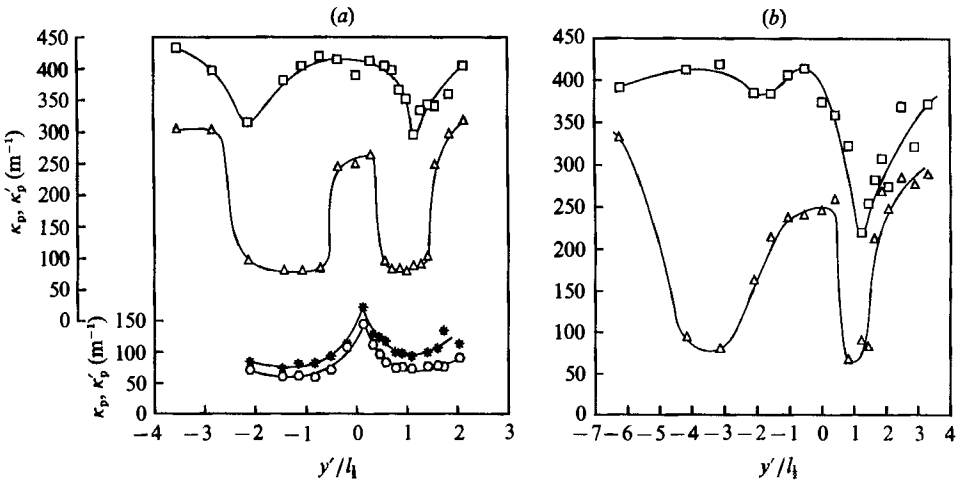

FIGURE 18. The wavenumber at which the temperature spectra peak as a function of lateral distance across the plume. (*a*) 3.3:1 parallel bar grid. □, unconditioned spectrum peak; △, conditioned spectrum peak at $x'/x_0 = 0.10$, $x_0 = 62.4$ cm; *, unconditioned spectrum peak; ○, conditioned spectrum peak at $x'/x_0 = 1.12$, $x_0 = 31.5$ cm. (*b*) 8.9:1 parallel bar grid, □, unconditioned spectrum peak; △, conditioned spectrum peak at $x'/x_0 = 0.10$, $x_0 = 62.4$ cm.

of $y' = 0$. This indicates that the Lagrangian integral timescales are approximately equal on both sides of the mixing layer. It was shown in VW (figure 10*b*) that the Eulerian timescale is approximately constant across the mixing layer also and thus the above result is consistent with the normal assumption (Tennekes & Lumley 1972) of the equality of the Eulerian and Lagrangian timescales.

The qualitative agreement between κ_p and κ_p' at $x'/x_0 = 1.12$ (figure 18*a*) is very good. Here too, κ_p' lies below κ_p, however, the difference is not as large as that for $x'/x_0 = 0.10$, because at $x'/x_0 = 1.12$, the instantaneous plume width is comparable to the convective lengthscales.

Figure 18*b* shows profiles of κ_p and κ_p' at $x'/x_0 = 0.10$ ($x_0 = 62.4$ cm), for the 8.9:1 bar grid. The similarity between the profile of κ_p' here and that for the 3.3:1 bar grid at $x'/x_0 = 0.10$ is remarkable. It is interesting to note that the change in the magnitude of κ_p' for these two grids at $x'/x_0 = 0.10$, is also nearly identical because the Eulerian (and presumably the Lagrangian) integral timescales are approximately the same (table 1), even though the length and velocity scales are different. The profile of κ_p, however, is very different from the corresponding profile for the 3.3:1 bar grid. The profile of κ_p in figure 18(*b*) is highly asymmetric, with larger variations in the region of $y' > 0$. This is because in the region of $y' < 0$ the high frequency jiggling of the instantaneous plume caused by fluctuations originating from the large-scale side is vigorous and dominates over the flapping frequency thus maintaining a large value for κ_p even at the trough of κ_p'. On the other hand, for $y' > 0$, jiggling is caused by fluctuations from the small-scale side which are of a lower wavenumber (since the turbulent Reynolds number is much smaller here, table 1) and thus the behaviour of κ_p' dominates the overall spectrum, causing κ_p to dip down in the trough region of κ_p'. The ratio of the Kolmogorov timescales is approximately 14 and that of the Kolmogorov lengthscales is approximately 3.75. The corresponding ratios for the 3.3:1 grid are only 2.5 and 1.6 respectively, thus yielding a nearly symmetric κ_p profile (figure 18*a*).

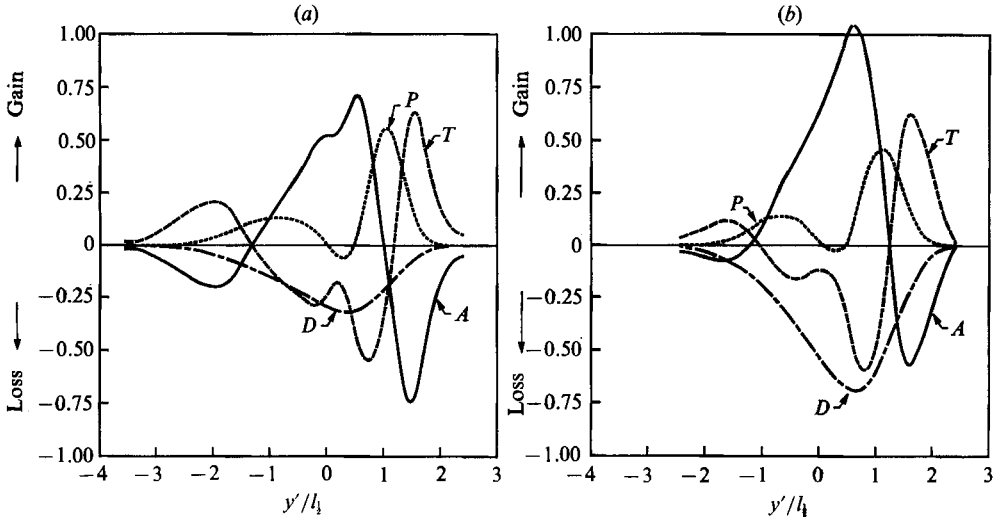

FIGURE 19. The temperature variance budget (equation (6)) for the line source; 3.3:1 parallel bar grid. Labels and normalization are the same as for figure 11. (*a*) $x'/x_0 = 0.10$, x_0 62.4 cm, (*b*) $x'/x_0 = 1.12$, x_0 31.5 cm.

5.2.3. *The temperature variance budget*

Figure 19(*a*, *b*) shows normalized temperature variance budgets obtained at $x'/x_0 = 0.10$ ($x_0 = 62.4$ cm) and $x'/x_0 = 1.12$ ($x_0 = 31.5$ cm) respectively, for the line source spreading in the shearless turbulence mixing layer generated by the 3.3:1 bar grid. The ordinate has been non-dimensionalized by $\Theta^2_{\max} U/x$ and the abscissa by $l_{\frac{1}{2}}$. The procedure used in generating these budgets was identical to the one outlined in §5.1.3 above. The accuracy of this method is investigated in Appendix A, wherein the temperature variance profile at $x'/x_0 = 1.21$ has been evaluated using the variance profile and the advection term at $x'/x_0 = 1.12$; the agreement between the estimate for and the experimental measurements of the temperature variance at $x'/x_0 = 1.21$ (figure 22), is extremely good.

These budgets exhibit some similarities with those presented in §5.1. Here also we find that at the outer edges of the mean plume, the transport term does not drop to zero as quickly as the destruction and production terms and it is balanced by the advection term there. In the central region, the transport and production terms are approximately in balance and the destruction term is balanced by advection. Note that the normalized magnitude of the destruction term nearly triples as x'/x_0 is increased from 0.10 (figure 19*a*) to 1.12 (figure 19*b*) and the advection term increases significantly also.

However, unlike the budgets presented in figure 11 (*a*, *b*) the profiles here are highly asymmetric about the origin y_0, at both values of x'/x_0. The positive peak of the transport term for $y' > 0$ is three times as large as that attained when $y' < 0$ at $x'/x_0 = 0.10$ and nearly five times as large at $x'/x_0 = 1.12$. Similar ratios for the production term are 4 and 3 respectively. It is interesting to note that for $x'/x_0 = 0.10$, while the ratio of the positive peaks of the transport term is approximately 3, the integral of the transport term over the region where it is positive and $y' > 0$ is only 1.5 times as large as the corresponding (positive) integral evaluated for $y' < 0$, owing to the much larger spread of the mean plume for $y' < 0$.

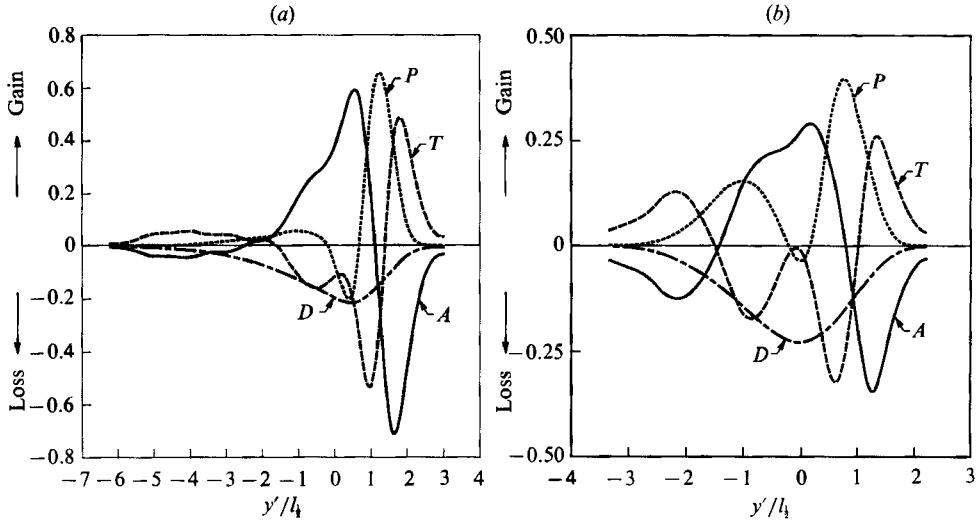

FIGURE 20. The line source temperature variance budget for the 8.9:1 parallel bar grid and 3:1 perforated plate. Labels and normalization are the same as for figure 11. (*a*) 8.9:1 parallel bar grid, (*b*) 3:1 perforated plate, both at $x'/x_0 = 0.10$, $x_0 = 62.4$ cm.

A similar calculation at $x'/x_0 = 1.12$ yields a ratio of 4. For the production term the corresponding ratios are 1.9 at $x'/x_0 = 0.10$ and 2.5 at $x'/x_0 = 1.12$.

The production term in figure 19(*a*) is slightly negative in the neighbourhood of $y' = 0$, indicating a region of counter-gradient flux. Although this region is small, it is statistically significant since the points where the $\overline{\theta v}$ and $\partial\Theta/\partial y$ profiles change sign can be determined to within 0.5 mm while the region of counter gradient flux is three times as large. As shown below (figure 20), the budgets for the 8.9:1 bar grid and the 3:1 perforated plate, corroborate the presence of counter-gradient flux. At $x'/x_0 = 1.12$ (figure 19*b*) this region of negative production almost disappears and presumably, further downstream, when turbulent-diffusion is the dominant spreading mechanism, counter-gradient flux would be absent together. In Appendix B, using a simple flapping-plume model it is shown that such a region of negative production is necessarily present in the turbulent-convective regime of a line source spreading in inhomogeneous turbulence.

Figure 20(*a*, *b*) shows budgets for the 8.9:1 bar grid and the 3:1 perforated plate respectively, at $x'/x_0 = 0.10$ ($x_0 = 62.4$ cm). The qualitative similarity between these budgets and that in figure 19(*a*) is striking. As expected, the asymmetry of the profiles in figure 20(*a*) is much larger compared with that of figure 19(*a*). These budgets, especially that of the 8.9:1 bar grid, also show a region of counter-gradient flux in the vicinity of $y' = 0$.

5.2.4. *The heat flux budget*

The evolution equation for the principal component of the heat flux vector is given in §2 (equation (7)). Figure 21 shows a balance between the various terms described in equation (7), for the 3.3:1 bar grid at $x'/x_0 = 1.12$. The transport and production terms were determined in a manner similar to the one used in determining the variance budgets. In order to determine $\partial\overline{\theta v}/\partial x$ and hence the advection term, two sets of measurements of $\overline{\theta v}$ were made approximately one mesh length apart in the longitudinal direction. The locations were $x_1'/x_0 = 1.12$ ($x_1 = 21.2M_2$) and $x_2'/x_0 =$

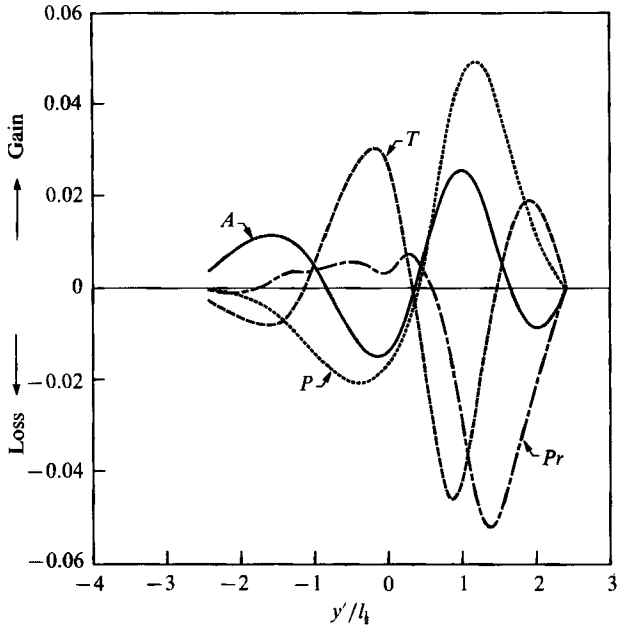

FIGURE 21. The line source heat flux (equation (7)) budget for the 3.3:1 parallel bar grid. $x_0 = 31.5$ cm, $x'/x_0 = 1.12$. The ordinate values have been normalized by $(\Theta_{\max} U^2)/x'$. The labels indicated in the figure are: A, normalized advection; P, normalized production; T, normalized transport and Pr, normalized pressure.

1.21 ($x_2 = 22.1 M_2$). Smooth curves were faired through the data points using interpolating splines and the gradient was determined using a linear fit. The pressure term could not be measured and was obtained from the balance of the other terms. Before discussing the budget it should be noted that the advection term so estimated, is likely to possess large errors, partly because it is determined from a small difference between two large values and partly because of errors in probe position. If we assume that the fractional error in $\overline{\theta v}$ is approximately 3%, then the error in $\partial\overline{\theta v}/\partial x$ could be as large as 50%. Secondly, because of the large gradients in the $\overline{\theta v}$ profiles (figure 15*c*) a lateral shift of 0.5 mm in one of the profiles could cause the zero crossings of the advection term to shift by as much as 5 mm ($0.25 l_{\frac{1}{2}}$), and change the magnitude of its peaks by as much as 50%. Thus only qualitative information can be extracted from figure 21.

Given the qualifications mentioned above, the $\overline{\theta v}$ budget indicates that advection and transport are approximately in balance across the whole plume. Consequently, the pressure term is responsible for the destruction of $\overline{\theta v}$ and approximately balances the production term. This is consistent with the results of Wyngaard & Weil (1990) where it is shown that a simple eddy diffusivity model applied to the $\overline{\theta v}$ and $\overline{\theta v^2}$ equations, yields the balance described above.

6. Conclusions

We have shown that thermal dispersion from a line source in the shearless turbulence mixing layer is highly asymmetrical because of the variation of turbulence intensity throughout the layer. The measurements were carried out with the line source placed at approximately the inflection point of the kinetic energy profile but

the same qualitative features would be observed if the source were placed off centre although the effects of the large (or small) scale would be more pronounced initially depending on whether the source were placed closer to the high (or low) turbulence intensity side of the mixing layer. The line source was placed at two downstream locations; 31.5 cm and 62.4 cm from the grid and the measurements were carried out in the turbulent convective region where both flapping and fine-scale internal structure of the plume are important in the mixing process. We have examined spectra and thermal budgets to highlight these processes and the results are compared with new measurements of spectra and budgets for a line source in homogeneous decaying grid turbulence. Special care has been taken to document the velocity field in order to aid modelling of the dispersion process. Thus the velocity field on both sides of the mixing layer has been completely specified (table 1 and VW) and the p.d.f. as well as the variance and skewness profiles at the approximate location of the second line source (62.4 cm) is given (figures 3 and 4). Furthermore, the second, third and fourth moment profiles at both locations of the line source studied here can be inferred from the scaled data in figures 9, 11 and 12 of VW. Our main findings are as follows.

In the convective range the mean temperature profiles are strongly skewed with a long tail extending into the low-turbulence side of the mixing layer (figure 12). Here the median and peak of the temperature distribution are deflected towards the large-scale turbulence region. As the plume evolves the profiles tend to become more symmetric as the internal structure of the instantaneous plume develops and becomes as significant as flapping motion in determining the overall plume structure. Our measurements only extend to the end of the convective range but the results suggest (figure 13) that in the diffusive range the mean temperature distribution would again become asymmetric with the longer tail now extending into the high-turbulence side of the mixing layer. Here turbulent diffusion (rather than flapping) assumes the dominant role and thus mixing will be more efficient in the high-turbulence side where the eddy diffusivity is larger. The temperature variance profiles (figure 14) are also asymmetric in the convective region. Just like the mean profiles, they tend to become more symmetric as the flow evolves, however as the diffusive range is approached an asymmetric double peak is observed. (In homogeneous grid turbulence a symmetric double peak is observed here (Warhaft 1984).) The ratio of the r.m.s. to mean centreline temperature rises to a maximum value of 1.4 close to the source and then declines to a value of approximately 1 at the end of the convective region; a result similar to the homogeneous case.

In order to summarize the temperature spectra and budget measurements we will first describe measurements of these quantities for the line source in decaying homogeneous grid turbulence. We note that these statistics have not been investigated previously for the homogeneous case. These will then be contrasted with the thermal field in the inhomogeneous mixing layer.

6.1. *Homogeneous grid turbulence*

Temperature spectra were calculated both from the raw time series (unconditioned spectrum) and the intermittency function (conditioned spectra). As the probe was traversed laterally across the plume the peaks of these spectra showed a characteristic W shape (figure 9*a*) with high wavenumber peaks at the centre and edge of the plume (where the time series showed the probe was nearly all the time in (or out) of the plume, interspersed with short blips) and low wavenumber peaks in the intermediate region where the probe spent approximately equal times inside and outside the

plume. The peaks of the spectra of the intermittency function (which highlight the flapping) had a similar form to the unconditioned spectra. However as the diffusive region was approached the peaks of the unconditioned spectra tended to show weaker wavenumber dependence in the central region of the plume since internal structure becomes more pronounced than flapping here (figure 9*a*). For both the conditioned and unconditioned time series the spectra were not self similar across the plume.

The temperature variance budget showed that production and transport have equal magnitude (and opposite sign) in the centre of the plume while advection balanced destruction (figure 11). Near the edge of the plume production and destruction approached zero rapidly and transport and advection were in balance. As the plume evolved the relative importance of these terms changed as the fine structure within the plume developed.

6.2. *The inhomogeneous mixing layer*

Here, too, the peak of the unconditioned and conditioned spectra showed a W shape as the plume was traversed (figure 18), however the trough was narrower on the high-turbulence side of the plume and the graphs of the conditioned and unconditioned spectral peaks were less congruent. The variation in wavenumber of the spectral peak was the same on the high- and low-turbulence sides of the plume for the intermittency spectrum but for the unconditioned spectrum there was less variation in the wavenumber peak on the low-turbulence side of the mixing layer than on the high-turbulence side, particularly for the 8.9:1 grid (figure 18*a*, *b*). This is understood by noting that the conditioned or intermittency spectra are determined largely by the turbulence integral timescale which remains approximately constant across the mixing layer (VW, figure 10*b*) while the unconditioned spectra are determined by a combination of large and small scales, the latter determining the fine-scale structure of the plume. The size of the small scales (Kolmogorov scale) varies across the mixing layer thereby affecting the fine structure of the plume and the form of the unconditioned spectrum from one side to the other.

As for the homogeneous case the temperature variance budget shows that advection balances transport in the outer edges of the plume where destruction and production are approximately zero. In the central region advection and dissipation are in rough balance (figure 18). However, the profiles of the budgets are highly asymmetric. A particularly interesting finding is that there is a significant region of counter gradient heat flux (negative production) in the central region of the mean plume. Using a simple flapping model it is shown that this is a consequence of the asymmetry of the velocity p.d.f. Presumably such regions should occur in the outer region of a turbulent boundary layer mixing with free-stream turbulence. The transverse ($\overline{\theta v}$) heat flux budget (not measured for the homogeneous case) also showed strong asymmetry. Here advection and transport were in approximate balance across the whole plume suggesting that the pressure term is in balance with production but this budget is less reliable than that for the temperature variance.

Finally we have shown that the measurements of the inhomogeneous plume, most extensively done using the 3.3:1 parallel bar grid, when contrasted with measurements done using the 8.9:1 grid and the perforated plate, show expected variations, with larger asymmetries in the plume occurring for the larger turbulence scale ratios across the mixing layer (figures 19 and 20).

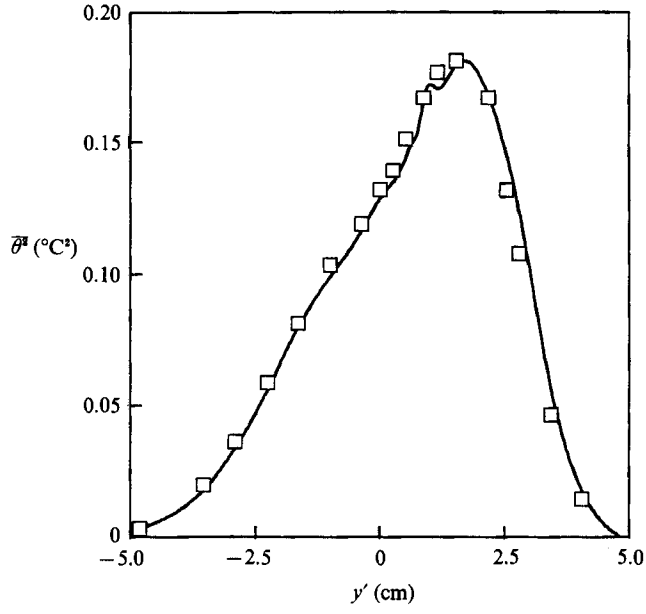

FIGURE 22. Temperature variance at $x'/x_0 = 1.21$, $x_0 = 31.5$ calculated from equation (A 1) (solid line) and measured (square symbols). 3.3:1 parallel bar grid.

We again thank Mr E. P. Jordan for his fine technical assistance. This work was supported by grants from the Department of Energy (Basic Energy Sciences DE-FG02-88ER13929) and the US National Science Foundation (Atmospheric Sciences ATM-8412558).

Appendix A

Figure 22 shows an attempt to ascertain the validity of the curve fitting and discrete differentiation procedures used in obtaining the scalar variance budgets shown in figures 11(*a*, *b*), 19(*a*, *b*), 20(*a*, *b*). The temperature variance profile for the 3.3:1 bar grid, at $x_2'/x_0 = 1.21$ was evaluated from that at $x_1'/x_0 = 1.12$ as,

$$\overline{\theta^2}(x_2', y') = \overline{\theta^2}(x_1', y') + (x_2' - x_1')\left.\frac{\partial \overline{\theta^2}}{\partial x'}\right|_{(x_1', y')}, \tag{A 1}$$

where, the scalar variance gradient, $\partial\overline{\theta^2}/\partial x'$, was determined from the advection term at $x_1'/x_0 = 1.12$, which in turn was estimated from the variance budget (figure 19*a*). The temperature variance calculated using equation (A 1), is represented by the solid line in figure 22, while, the symbols indicate experimental points obtained at $x_1'/x_0 = 1.12$. We note that the agreement between the curve and the data points is extremely good.

Appendix B

The flapping plume model was first proposed by Taylor (1921) to describe the spreading of scalar contaminants close to the source. It was refined by Townsend (1954) and Saffman (1960). Here, we will be using the form presented in Lumley & Van Cruyningen (1985), since it enables one to calculate entire moment profiles,

instead of just the mean spreading rates. In the analysis that follows, the downstream distance from the source is fixed (say x').

Let $g(y'-Y)$ represent the temperature distribution in the instantaneous plume centred at Y, and let $f(Y)\,\mathrm{d}Y$ be the probability of finding the centre in the interval $[Y, Y+\mathrm{d}Y)$, then the mean temperature distribution $\langle\Theta\rangle$ (angle brackets will be used to denote mean quantities here) is given by,

$$\langle\Theta(y')\rangle = \int_{-\infty}^{\infty} g(y'-Y)f(Y)\,\mathrm{d}Y. \tag{B 1}$$

Similarly, moments of the fluctuating temperature θ may be obtained as,

$$\begin{aligned}\langle\theta^2(y')\rangle &= \langle\theta'^2(y')\rangle - \langle\Theta(y')\rangle^2 \\ &= \int_{-\infty}^{\infty} g^2(y'-Y)f(Y)\,\mathrm{d}Y - \left[\int_{-\infty}^{\infty} g(y'-Y)f(Y)\,\mathrm{d}Y\right]^2, \end{aligned}\tag{B 2}$$

$$\vdots$$

$$\begin{aligned}\langle\theta^n(y')\rangle &= \langle\theta'^n(y')\rangle - {}^nC_1\langle\theta^{n-1}(y')\rangle\langle\Theta(y')\rangle - \dots \\ &\quad - {}^nC_r\langle\theta^{n-r}(y')\rangle\langle\Theta(y')\rangle^r - \dots - \langle\Theta(y')\rangle^n, \end{aligned}\tag{B 3}$$

where θ' is the instantaneous temperature.

In homogeneous turbulence both f and g may be well approximated by Gaussian distributions. In inhomogeneous turbulence, the instantaneous temperature distribution initially remains Gaussian (since the source size is smaller than the Kolmogorov lengthscale and molecular diffusion is principally responsible for the spreading of the instantaneous plume close to the source), however, f is no longer a Gaussian distribution. Close to the source it is reasonable to assume that the Lagrangian velocity auto-correlation does not depart significantly from unity, thus,

$$f(Y) = f_v(v')/t', \tag{B 4}$$

where, $f_v(v')$ is the p.d.f. of v fluctuations at the source, t' is the mean convection time x'/U and $v' \approx Y/t'$.

Figure 23 shows $f_v(v')$ at $x = 21.2M_2$ and $y' = 0$ for the 3.3:1 bar grid. The profile is asymmetric and difficult to represent analytically. Let us assume that the p.d.f. can be represented as the sum of two half Gaussian distributions, one corresponding to each velocity scale, matched at the peak. As shown in figure 23, this is a good assumption to the right of the peak but not so good to the left of it. However, in the discussion to follow, it is the asymmetry of the p.d.f. about the peak that is of relevance, not the exact form, thus for analytic simplicity let us assume the following:

$$f(Y) \approx \begin{cases} \dfrac{2}{(2\pi)^{\frac{1}{2}}(\sigma_1+\sigma_2)}\exp\left[-\dfrac{(Y-y_\mathrm{p})^2}{2\sigma_2^2}\right] & (Y < y_\mathrm{p}), \\ \dfrac{2}{(2\pi)^{\frac{1}{2}}(\sigma_1+\sigma_2)}\exp\left[-\dfrac{(Y-y_\mathrm{p})^2}{2\sigma_1^2}\right] & (Y > y_\mathrm{p}). \end{cases} \tag{B 5}$$

The origin of Y coincides with the source location y_0. y_p is the location of the peak of the distribution and is given by,

$$y_\mathrm{p} = 2(\sigma_2-\sigma_1)/(2\pi)^{\frac{1}{2}}, \tag{B 6}$$

and σ_1 and σ_2 are given by

$$\sigma_1 = (\overline{v_1^2})^{\frac{1}{2}}t', \quad \sigma_2 = (\overline{v_2^2})^{\frac{1}{2}}t'. \tag{B 7}$$

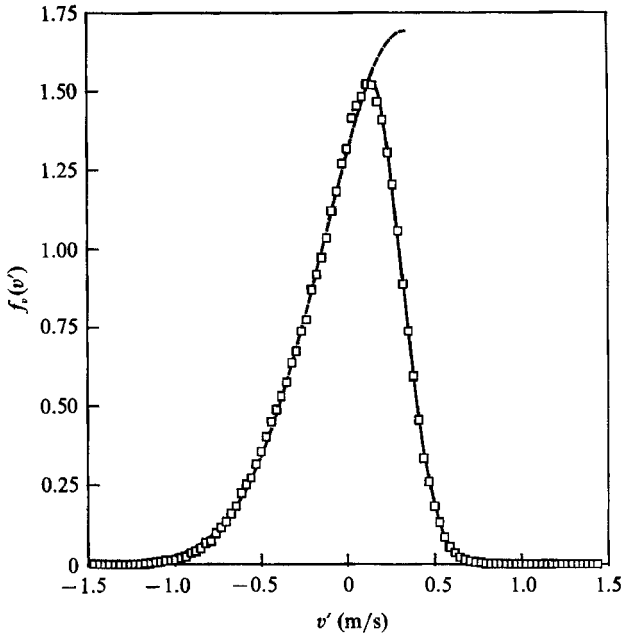

FIGURE 23. A Gaussian fit to each side of the p.d.f. of the data of figure 4(*a*).

Let the standard deviation of the instantaneous temperature profile be σ_p and let the peak temperature be Θ_p, then,

$$g'(y'-Y) = \Theta_p \exp\left[-\frac{(y'-Y)^2}{2\sigma_p^2}\right]. \tag{B 8}$$

If we assume further, that $\sigma_p \ll \sigma_1$ and $\sigma_p \ll \sigma_2$, then $\langle\Theta\rangle$, $\langle\theta v\rangle$ and $-\langle\theta v\rangle\partial\langle\Theta\rangle/\partial y$ can be easily evaluated as,

$$\langle\Theta(y')\rangle = \begin{cases} \dfrac{2\Theta_p\sigma_p}{(\sigma_1+\sigma_2)}\exp\left[-\dfrac{(y'-y_p)^2}{2\sigma_2^2}\right] & (y' < y_p), \\ \dfrac{2\Theta_p\sigma_p}{(\sigma_1+\sigma_2)}\exp\left[-\dfrac{(y'-y_p)^2}{2\sigma_1^2}\right] & (y' > y_p), \end{cases} \tag{B 9}$$

and

$$\langle\theta v\rangle = \begin{cases} \dfrac{2\Theta_p\sigma_p}{(\sigma_1+\sigma_2)}\dfrac{y'}{t'}\exp\left[-\dfrac{(y'-y_p)^2}{2\sigma^2}\right] & (y' < y_p), \\ \dfrac{2\Theta_p\sigma_p}{(\sigma_1+\sigma_2)}\dfrac{y'}{t'}\exp\left[-\dfrac{(y'-y_p)^2}{2\sigma_1^2}\right] & (y' > y_p), \end{cases} \tag{B 10}$$

thus,

$$-\langle\theta v\rangle\frac{\partial\langle\Theta\rangle}{\partial y'} = \begin{cases} \left(\dfrac{2\Theta_p\sigma_p}{(\sigma_1+\sigma_2)}\right)^2\dfrac{(y'-y_p)y'}{t'\sigma_2^2}\exp\left[-\dfrac{(y'-y_p)^2}{2\sigma_2^2}\right] & (y' < y_p), \\ \left(\dfrac{2\Theta_p\sigma_p}{(\sigma_1+\sigma_2)}\right)^2\dfrac{(y'-y_p)y'}{t'\sigma_1^2}\exp\left[-\dfrac{(y'-y_p)^2}{2\sigma_1^2}\right] & (y' > y_p), \end{cases} \tag{B 11}$$

For the flows considered here $\sigma_2 > \sigma_1$ (the large-scale homogeneous region corresponds to $y' \to \infty$) hence $y_p > 0$ (see equation (B 6)). Equation (B 11) then indicates that there is a region of negative production when $0 < y' < y_p$. Note that this result is independent of the actual form of $f(Y)$ since $\langle \theta v \rangle$ changes sign at $y' = 0$, while $\partial \langle \theta \rangle / \partial y$ changes sign at $y' = y_p$ thus yielding a region of negative production (or counter-gradient flux) for $0 < y' < y_p$.

REFERENCES

ANAND, M. S. & POPE, S. B. 1983 Diffusion behind a line source in grid turbulence. In *Turbulent Shear Flows* (ed. L. J. S. Bradbury, F. Durst, B. E. Launder, F. W. Schmidt & T. H. Whitelaw), vol. 4, pp. 46–61. Springer.

CHAMPAGNE, F. H. & SLEICHER, C. A. 1967 Turbulence measurements with inclined hot-wires. Part 2. How-wire response equations. *J. Fluid Mech.* **28**, 177–182.

CHAMPAGNE, F. H., SLEICHER, C. A. & WEHRMANN, O. H. 1967 Turbulence measurements with inclined hot-wires. Part 1. Heat transfer experiments with inclined hot-wire. *J. Fluid Mech.* **28**, 153–176.

CHATWIN, P. C. & SULLIVAN, P. J. 1989 The intermittency factor of scalars in turbulence. *Phys. Fluids* A **1**, 761–763.

FACKRELL, J. E. & ROBINS, A. G. 1982 Concentration fluctuations and fluxes in plumes from point sources in a turbulent boundary layer. *J. Fluid Mech.* **117**, 1–26.

FREYMUTH, P. & UBEROI, M. S. 1971 Structure of temperature fluctuations in the turbulent wake behind a heated cylinder. *Phys. Fluids* **14**, 2574–2580.

FREYMUTH, P. & UBEROI, M. S. 1973 Temperature fluctuations in the turbulent wake behind an optically heated sphere. *Phys. Fluids* **16**, 161–168.

GILBERT, B. 1980 Diffusion mixing in grid turbulence without mean shear. *J. Fluid Mech.* **100**, 349–365.

HUNT, J. C. R. 1982 Diffusion in the stable boundary layer. In *Atmospheric Turbulence and Air Pollution Modelling* (ed. F. T. M. Nieuwstadt & H. van Dop), pp. 231–274. D. Reidel.

HUNT, J. C. R. 1985 Turbulent diffusion from sources in complex flows. *Ann. Rev. Fluid Mech.* **17**, 447–485.

KARNIK, U. & TAVOULARIS, S. 1989 Measurements of heat diffusion from a continuous line source in a uniformly sheared turbulent flow. *J. Fluid Mech.* **202**, 233–261.

KELLOGG, R. M. & CORRSIN, S. 1980 Evolution of a spectrally local disturbance in grid-generated, nearly isotropic turbulence. *J. Fluid Mech.* **96**, 641–669.

LAMB, R. G. 1982 Diffusion in the convective boundary layer. In *Atmospheric Turbulence and Air Pollution Modelling* (ed. F. T. M. Nieuwstadt & H. van Dop), pp. 159–230. D. Reidel.

LUMLEY, J. L. & VAN CRUYNINGEN, I. 1985 Limitations of second order modeling of passive scalar diffusion. In *Frontiers in Fluid Mechanics* (ed. S. H. Davis & J. L. Lumley), pp. 199–218. Springer.

NAKAMURA, I., SAKAI, Y. & MIYATA, M. 1987 Diffusion of matter by a non-buoyant plume in grid turbulence. *J. Fluid Mech.* **178**, 379–403.

PERRY, A. E. 1982 *Hot Wire Anemometry.* Oxford University Press.

SAFFMAN, P. G. 1960 On the effect of the molecular diffusivity in turbulent diffusion. *J. Fluid Mech.* **8**, 273–283.

SIRIVAT, A. & WARHAFT, Z. 1983 The effect of a passive cross-stream temperature gradient on the evolution of temperature variance and heat flux in grid turbulence. *J. Fluid Mech.* **128**, 323–346.

STAPOUNTZIS, H., SAWFORD, B. L., HUNT, J. C. R. & BRITTER, R. E. 1986 Structure of the temperature field downwind of a line source in grid turbulence. *J. Fluid Mech.* **165**, 401–424.

TAYLOR, G. I. 1921 Diffusion by continuous movements. *Proc. Lond. Math. Soc.* **20**, 196–212.

TAYLOR, G. I. 1935 Statistical theory of turbulence. IV. Diffusion in a turbulent air stream. *Proc. R. Soc. Lond.* A **151**, 465–478.

TENNEKES, H. & LUMLEY, J. L. 1972 *A First Course in Turbulence.* MIT Press.

TOWNSEND, A. A. 1954 The diffusion behind a line source in homogeneous turbulence. *Proc. R. Soc. Lond.* A **224**, 487–512.

UBEROI, M. S. & CORRSIN, S. 1953 Diffusion of heat from a line source in isotropic turbulence. *NACA Rep.* 1142.

VEERAVALLI, S. & WARHAFT, Z. 1989 The shearless turbulence mixing layer. *J. Fluid Mech.* **207**, 191–229.

WARHAFT, Z. 1984 The interference of thermal fields from line sources in grid turbulence. *J. Fluid Mech.* **144**, 363–387.

WARHAFT, Z. & LUMLEY, J. L. 1978 An experimental study of the decay of temperature fluctuations in grid turbulence. *J. Fluid Mech.* **88**, 659–684.

WYNGAARD, J. C. & WEIL, J. C. 1990 Transport asymmetry in skewed turbulence. Submitted to *Phys. Fluids.*

ZDRAVKOVICH, M. M. 1969 Smoke observations of the formation of a Kármán vortex street. *J. Fluid Mech.* **37**, 491–496.